



HAL
open science

In situ synthesis of Fe₃O₄ nanoparticles coated by chito-oligosaccharides: physico-chemical characterizations and cytotoxicity evaluation for biomedical applications

Paula Nunes de Oliveira, Amani Moussa, Nadège Milhau, Raquel Dosciatti Bini, Caroline Prouillac, Breno Ferraz de Oliveira, Gustavo Sanguino Dias, Ivair Aparecido Santos, Isabelle Morfin, Guillaume Sudre, et al.

► To cite this version:

Paula Nunes de Oliveira, Amani Moussa, Nadège Milhau, Raquel Dosciatti Bini, Caroline Prouillac, et al.. In situ synthesis of Fe₃O₄ nanoparticles coated by chito-oligosaccharides: physico-chemical characterizations and cytotoxicity evaluation for biomedical applications. *Nanotechnology*, 2020, 31 (17), pp.175602. 10.1088/1361-6528/ab68f9 . hal-02749772

HAL Id: hal-02749772

<https://univ-lyon1.hal.science/hal-02749772>

Submitted on 24 Mar 2021

HAL is a multi-disciplinary open access archive for the deposit and dissemination of scientific research documents, whether they are published or not. The documents may come from teaching and research institutions in France or abroad, or from public or private research centers.

L'archive ouverte pluridisciplinaire **HAL**, est destinée au dépôt et à la diffusion de documents scientifiques de niveau recherche, publiés ou non, émanant des établissements d'enseignement et de recherche français ou étrangers, des laboratoires publics ou privés.

***In situ* synthesis of Fe₃O₄ nanoparticles coated by chito-oligosaccharides: physico-chemical characterizations and cytotoxicity evaluation for biomedical applications**

Paula Nunes de Oliveira^{*1}, Amani Moussa¹, Nadège Milhau², Raquel Dosciatti Bini³, Caroline Prouillac², Breno Ferraz de Oliveira³, Gustavo Sanguino Dias³, Ivair Aparecido Santos³, Isabelle Morfin⁴, Guillaume Sudre¹, Pierre Alcouffe¹, Thierry Delair¹, Luiz Fernando Cótica³, Stéphane Trombotto¹, Didier Pin², Laurent David¹

¹IMP, CNRS UMR 5223, Univ Claude Bernard Lyon 1, Univ Lyon, 15 bd Lataret, 69622 Villeurbanne, FR

²Univ Lyon, VetAgro Sup, UP ICE, F-69280 Marcy L'Etoile, FR

³Department of Physics, State University of Maringá, Av. Colombo, 5790, Maringá, Paraná, 87020-900, BR

⁴Université Grenoble Alpes, LiPhy, 38000 Grenoble FR

E-mail: paulaoliveiraqmc@gmail.com

Published in Nanotechnology:

In Situ Synthesis of Fe₃O₄ Nanoparticles Coated by Chito-Oligosaccharides: Physico-Chemical Characterizations and Cytotoxicity Evaluation for Biomedical Applications. **Oliveira P., Moussa A., Milhau N., Dosciatti Bini R., Prouillac C., Ferraz de Oliveira B., Dias G., Santos I., Morfin I., Sudre G., Alcouffe P., Delair T., Cótica L., Trombotto S., Pin D., David L.**, *Nanotechnology*, 2020, 31, 175602.

Link to the publisher version: <https://doi.org/10.1088/1361-6528/ab68f9>

Creative Commons Attribution Non-Commercial No Derivatives License

Abstract

Fe₃O₄ nanoparticles coated with chito-oligosaccharides (COS) were prepared *in situ* by a simple co-precipitation method through a mixing of iron ions (Fe³⁺ and Fe²⁺) and COS aqueous solutions followed by precipitation with ammonia. The impact of COS with different degree of polymerization (DP 10, 24 and 45) and degree of *N*-acetylation (DA) ~ 24 and 50 % (exhibiting high solubility) on the synthesis and physical properties of the coated magnetic nanoparticles was evaluated. Several advantages were found when the magnetic nanoparticles were prepared in the presence of the studied COSs, such as: preparation of functionalized magnetic nanoparticles with narrower size distributions and, consequently, higher saturation magnetization (an increase of up to 22%); and an expressive increasing in the concentration of COS-coated magnetic nanoparticles (up to twice) in the cell viability test in comparison with pure Fe₃O₄ nanoparticles. Furthermore, among the analyzed samples, the magnetic nanoparticles coated by COS with DA ~ 50 % present a higher cytocompatibility. Our results allow envisioning various biomedical applications, valorizing the use of coated-magnetic nanoparticles for magnetic-field assisted drug delivery, enzyme or cell immobilization, or as a marker for specific cell tracking, among others.

Keywords: Chito-oligosaccharides, magnetic nanoparticles, biomedical applications, co-precipitation

1. Introduction

Nanoparticles (NPs) are known as those in which at least one dimension ranges up to 100 nm, resulting in a high surface area to volume ratio [1]. Generally, they show different physico-chemical behaviors when compared to the bulk and can be used in several applications [2, 3]. Thanks to recent evolution and demands in nanobiotechnologies, magnetic nanoparticles (MNPs) have attracted increasing attention [3-5]. This is because they have a great potential to improve conventional therapeutic procedures and traditional clinical diagnostics, introducing novel approaches in biomedicine and tissue engineering. [6-10]. The most frequently used magnetic nanomaterials are iron oxide nanoparticles, comprising magnetite (Fe_3O_4) and maghemite ($\gamma\text{-Fe}_2\text{O}_3$) due to their low toxicity [8, 11]. They possess different physico-chemical properties originating from the difference in their iron oxidation states. Fe_3O_4 differs from most other iron oxide, once it contains both divalent and trivalent iron ions. Fe_3O_4 has a cubic inverse spinel structure in a close packed array of oxide ions [12]. The octahedral sites within the unit cell are randomly occupied by approximately equal numbers of Fe^{3+} and Fe^{2+} ions, while the tetrahedral sites are occupied exclusively by the smaller Fe^{3+} ions and, in stoichiometric magnetite, the $\text{Fe}^{2+}/\text{Fe}^{3+}$ ratio is $\sim 1/2$ [12, 13]. Magnetite displays both *n*-type and *p*-type semiconductor behavior with a Fermi level in a low-mobility spin-polarized *3d* band. Fe_3O_4 possesses low band gap energy (0.1 eV) and consequently exhibits the lowest resistivity among the metal oxides ($\sim 5 \cdot 10^{-5} \Omega \cdot \text{m}$ [14]), a property attributable to the rapid exchange of electrons between Fe^{2+} and Fe^{3+} in octahedral sites [12, 13].

Some of the physico-chemical properties of the MNPs, such as their magnetic properties, are impacted by their size and shape [15]. A desired magnetic state for these NPs is the superparamagnetic one, *i.e.*, the magnetization of the NPs can be saturated under a very low external magnetic field, but in the absence of this field, their net magnetic moments are randomized to zero [13, 15]. Once exposed to an external magnetic field, the superparamagnetic NPs moments can align along the field direction, achieving magnetic saturation at a magnitude that far exceeds that from any of the known biological entities. This unique property of superparamagnetic NPs allows not only the detection of them within biological samples, but also the easy manipulation of the biological components with an external magnetic field [5, 16]. In general, magnetite NPs show this property when their sizes are smaller than 20 nm in diameter and this is exploited for their dispersion in physiological solutions, facilitating the MNPs coupling with biological agents [17, 18].

Although very small particles are ideal for biological applications, they have high surface energy resulting from their large surface to volume ratio [13]. This effect can induce NPs aggregation, even for MNPs that are superparamagnetic, resulting in the formation of large clusters which limits their bio-applications [13]. To avoid this aggregation, MNPs are usually coated to promote their colloidal stability, water dispersibility and also provide bio and chemical functionality with the coupling of bioactive molecules [3, 11, 19]. The use of suitable coatings can also minimize precipitation and the formation of agglomerates, prolonging the circulation time when applied *in vivo* and decreasing the cytotoxicity [9, 20-22]. In fact, many researchers have used silica, carbon, and biopolymers to modify the Fe_3O_4 nanoparticle surfaces [19, 23, 24].

As an interesting alternative for MNPs coating, chitosan is a well-known natural amino-polysaccharide that has drawn interest due to its unique properties, *e.g.*, it is non-toxic, biocompatible, biodegradable, and anti-bacterial [25]. A significant advantage of chitosan is the reactive amino and hydroxyl groups offering many active sites to conjugate with organic groups and/or complex different metals [26]. Chitosan and its derivatives have been widely envisioned in many applications, including gene and drug delivery, tissue repair, water purification and cosmetics [27]. Unfortunately, some chitosan applications are affected by its viscous solutions (due to high molar mass), its solubility limited to diluted acid aqueous media (*i.e.*, its poor solubility at neutral pH) [28]. In order to address these limitations, chito-oligosaccharides (COS), that are defined as the oligomer forms of chitosan or chitin prepared either chemically or enzymatically [28], have been investigated. COS maintain some of the original properties of chitosan, and they also provide water-solubility at neutral pH, non-toxicity, biocompatibility and unique physiological activities [29, 30]. They also exhibit antibacterial, antifungal and antitumor activities, as well as immuno-enhancing effects on animals [28, 31]. Few studies previously showed the preparation and application of Fe_3O_4 :COS NPs [32, 33], in which, in general, a Fe_3O_4 NPs suspension was prepared and subsequently a COS solution was added to the media, promoting the COS adsorption on the MNPs surface [34-36].

In this work, we innovatively propose the use of chito-oligosaccharides with controlled structure, derived from chitosan polymer as complexing agents, to assist the synthesis of magnetite NPs. Due to the interactions between the amino groups of COS and the iron ions, *in situ* functionalized COS-coated Fe₃O₄ nanoparticles could be prepared. Consequently, MNPs with narrow size distributions and improved chemical stability and biocompatibility were obtained. COS with different degrees of polymerization (DP, with narrow distribution) and degrees of *N*-acetylation (DA) *i.e.*, COS with DP/DA of 10/53, 24/24, 24/47 and 45/47, were synthesized by nitrous deamination and reacylation. In fact, they were tested to evaluate the impact of their structure on the properties of coated NPs. COS structures were precisely characterized by proton nuclear magnetic resonance spectroscopy (¹H NMR) and size exclusion chromatography (SEC-MALLS). COS-coated Fe₃O₄ NPs were synthesized by co-precipitation from an aqueous solution with mixed iron ions (Fe³⁺ and Fe²⁺) and COS. The resulting coated MNPs were characterized convergently with respect to their physico-chemical behavior and cytotoxicity following the methodology described below.

2. Experimental methods

2.1 Materials

Commercial chitosan (batch type 244/020208; degree of *N*-acetylation (DA) < 1%; $\overline{M}_w = 270$ kg/mol; $\overline{M}_n = 115$ kg/mol; $\overline{D} = 2.3$) was supplied by Mahtani Chitosan Ltd (Veraval, India) and characterized by ¹H NMR [37] and SEC-MALLS [38], as previously described. Iron(III) chloride hexahydrate (FeCl₃·6H₂O), iron(II) chloride tetrahydrate (FeCl₂·4H₂O), and aqueous ammonia (28%) were purchased from Sigma-Aldrich.

2.2 Synthesis procedures

2.2.1 Preparation of reduced low DA chito-oligosaccharides. Chitosan 244 (30 g, 187 mmole of D-glicosamine unit (GlcN)) was solubilized in 1 L of water by addition of 15.5 mL of HCl (37% w/w). A freshly prepared 25 mL of NaNO₂ aqueous solution was added to the chitosan solution at a GlcN/NaNO₂ molar ratio = 4, 10 and 30 to obtain COS₁₀ (DP ~ 10), COS₂₄ (DP ~ 24) and COS₄₅ (DP ~ 45), respectively. The reaction mediums were stirred for 12 h at room temperature. Then, NaBH₄ was added, at ~ 0 °C, in the COS₁₀ (125 mmols), COS₂₄ (48 mmols) and COS₄₅ (16 mmols) solutions. Additional stirring was performed for 12 h in these solutions to ensure the reduction of the aldehyde groups formed in chito-oligosaccharide-2,5-anhydrofuranose. For COS₁₀, the solution was neutralized by the addition of ammonium hydroxide solution (28% w/w) until pH ~ 8 then concentrated using a rotary evaporator. COS₁₀ was obtained as a white powder after precipitation in acetone, followed by several washings and finally dried under vacuum. COS₂₄ and COS₄₅ were precipitated by addition of ammonium hydroxide solution (28% w/w) to pH ~ 9, washed several times with deionized water until neutral pH and then freeze-dried. At the end, different samples were isolated: COS_{10/1}, COS_{24/0.7} and COS_{45/0.7} (labeled as COS_{DP/DA}), as a white powder with 70, 81 and 85 % mass yield, respectively. Full details about the characterization of the products are given in the Supporting Material.

2.2.2 *N*-acetylation of reduced chito-oligosaccharides. In order to increase the solubility of COS in the physico-chemical conditions of the precipitation of Fe₃O₄ NPs, *i.e.* at a basic pH, reacylated COS were prepared in homogeneous conditions [39]. The partial *N*-acetylation of low DA COS was performed by dissolving 0.5 g of each of the reduced chito-oligosaccharides in 20 mL of methanol/water 90:10 (v/v) for COS₁₀ and in 20 mL of methanol/acetic acid water (AcOH 1.5%(w/v)) 70:30 (v/v) and 50:50 (v/v) for COS₂₄ and COS₄₅, respectively, to ensure the solution homogeneity. Fresh acetic anhydride (76 and 149 μL) was added in a stoichiometric amount to reach the expected DA (~ 20 and 50%). After 14 h of stirring at room temperature, the solutions were neutralized by the addition of ammonia till pH ~8, and then concentrated by vacuum evaporation. The reaction solutions of the different *N*-acetylated chito-oligosaccharides COS_{10/53}, COS_{24/24}, COS_{24/47} and COS_{45/47} were precipitated, abundantly washed with acetone and finally dried under vacuum. This last step permits the removal of acetone and methanol along with other reaction impurities. At the end, the *N*-acetylated chito-oligosaccharides were produced in their free amine form as white powders with mass yields of 57, 62, 57 and 63 % for COS_{10/53}, COS_{24/24}, COS_{24/47} and COS_{45/47}, respectively. Their molecular characterization showed

that their molar mass distribution \mathcal{D} is rather narrow. The results for the calculations of \overline{DP} and \overline{DA} are given in Table 1 and details can be found in the Supporting Material (SM-Figures 1, 2 and 3).

2.2.3 Synthesis of Fe_3O_4 nanoparticles. The Fe_3O_4 NPs were prepared by the chemical co-precipitation route. Ferric chloride hexahydrate ($FeCl_3 \cdot 6H_2O$) and ferrous chloride tetrahydrate ($FeCl_2 \cdot 4H_2O$) were dissolved, at stoichiometric ratio 2:1, in deionized water under argon atmosphere and vigorous stirring at 60 °C. HCl (1 M) aqueous solution was added in to this salt solution to reach a final concentration of 0.1 M to stabilize the iron ions. Chemical precipitation was achieved by dropwise addition of NH_4OH solution (28%) to reach pH 10 under vigorous stirring. The precipitation of magnetite is visible from the immediate change of the color of reaction medium from dark orange to black. After continuously stirring for 1 h, the black precipitates of Fe_3O_4 were magnetically decanted and washed several times with deionized water. The Fe_3O_4 NPs were then dried in an oven under vacuum for 12 h at 50 °C.

Table 1 - Chito-oligosaccharides characterization, such as: average molar mass (\overline{Mw}), number average molar mass (\overline{Mn}), dispersity (\mathcal{D}), average number of GlcN repeating unit (\overline{DP}_n), and average degree of *N*-acetylation (\overline{DA}):

Samples $COS_{DP/DA}$	\overline{Mw}^a (kg/mol)	\overline{Mn}^a (kg/mol)	\mathcal{D}^a	\overline{DP}_n^b	\overline{DA}^b (%)
Chitosan244	270.00	115.00	2.30	714	1.00
$COS_{10/1}$	2.13	1.94	1.10	10	1.00
$COS_{24/0.7}$	5.74	4.42	1.30	24	0.70
$COS_{45/0.7}$	11.64	7.76	1.50	45	0.70
$COS_{10/53}$	3.10	2.50	1.20	-	53.00
$COS_{24/24}$	9.30	5.60	1.60	-	24.00
$COS_{24/47}$	11.80	7.40	1.58	-	47.00
$COS_{45/47}$	14.90	10.90	1.30	-	47.00

(a) \overline{Mw} , \overline{Mn} and \mathcal{D} were determined by SEC-MALLS in ammonium acetate; (b) the \overline{DP}_n and the \overline{DA} were determined by 1H NMR in D_2O at room temperature.

(b) The details about \overline{DP}_n and \overline{DA} calculus are given in the Supporting Material.

2.2.3 Synthesis of COS-coated Fe_3O_4 nanoparticles. COS-coated magnetite NPs were synthesized *in situ* by the co-precipitation of Fe^{2+} and Fe^{3+} salts in the presence of reacylated COS. The reacylated COS used in this study are listed in Table 1. First, 0.25 g of $COS_{DP/DA}$ ($COS_{10/53}$, $COS_{24/24}$, $COS_{24/47}$ and $COS_{45/47}$) was dissolved in 100 mL of deionized water. Iron salts (0.333 g of $FeCl_2 \cdot 4H_2O$ and 0.905 g of $FeCl_3 \cdot 6H_2O$) were dissolved in 20 mL of deionized water at 60 °C, under argon gas flow and vigorous stirring. 50 μ L of HCl (37 %) was added to this salt solution. Then, the COS solution was slowly added into the flask, still under argon atmosphere and mechanical stirring. After 1 h at 60 °C, 15 mL of ammonium hydroxide was added dropwise to the flask with continuous and vigorous stirring over the next 1 h (pH \cong 10). The colloidal COS-coated magnetite NPs were extensively washed with deionized water and separated by magnetic decantation. Finally, the obtained $Fe_3O_4:COS_{DP/DA}$ NPs (DP:DA of 10/53, 24/24, 24/47 AND 45/47) were dried in an oven (12 h, under vacuum at 50 °C) and stored at room temperature.

2.3 Characterization of COS and nanoparticles

2.3.1 1H NMR spectroscopy. Proton nuclear magnetic resonance spectroscopy (1H NMR) was recorded on a Bruker 500 MHz spectrometer at room temperature. All samples were dissolved at 10 mg/mL in D_2O with 5 μ L HCl 12 N, and transferred to 5 mm NMR tubes. Trimethylsilyl-3-propionic-2,2,3,3- D_4 acid sodium salt (99% atom D, TMSPA from Sigma-Aldrich, Saint-Quentin Fallavier, France) was used as internal reference (δ 0.00 for 1H).

2.3.2 Size-exclusion chromatography (SEC). SEC was performed on a chromatographic equipment composed of a 1260 Infinity Agilent Technologies pump connected to two TSK gel G2500 and G6000 columns (Tosoh Bioscience) in series. A multi-angle laser light scattering (MALLS) detector Dawn EOS (Wyatt Technology) operating at 664 nm was coupled on line to a Wyatt Optilab T-Rex differential refractometer. Sample solutions at 2-5 mg/mL were prepared and eluted in AcOH (0.2 M)/AcONH₄ (0.15 M) buffer (pH 4.5). Solutions were

previously filtered through 0.22 μm pore size membranes (Millipore) before injection. The eluent flow rate was 0.5 mL/min.

2.3.3 FT-IR spectroscopy. Infrared spectra were recorded with a Thermo Scientific Nicolet iS-10 FTIR spectrophotometer. The powder samples were ground with KBr and compressed into pellets. FT-IR spectra in the range 4000– 400 cm^{-1} were recorded by accumulation of 200 scans, with a resolution of 4 cm^{-1} . Infrared spectra were normalized using the more intense absorption band for COS spectra at 1070 cm^{-1} and for NPs spectra at 590 cm^{-1} .

2.3.4 Thermal characterization. The thermal degradation of COS, Fe_3O_4 and $\text{Fe}_3\text{O}_4\text{:COS}_{\text{DP/DA}}$ NPs were studied by thermogravimetric analysis (TA Instruments TGA-Q500). The TGA thermograms were recorded at a heating rate of 10 $^\circ\text{C}\cdot\text{min}^{-1}$ in the temperature range from 30 to 700 $^\circ\text{C}$ under dry air. The residual mass, in each case, was used to estimate the COS mass (organic material) on the NPs.

2.3.5 X-ray based characterizations

2.3.5.1 X-ray diffraction using laboratory source. The structure and composition of the magnetite nanoparticles (MNP) were examined by X-ray diffraction (XRD), using a Shimadzu XRD 7000 with Cu-K_α radiation equipped with counter monochromator, in the scattering angle 2θ from 15 $^\circ$ to 70 $^\circ$.

2.3.5.2 Wide-angle X-ray scattering. The crystalline structure of the synthesized NPs were also studied by two-dimensional wide-angle X-ray scattering (2D-WAXS) measurements performed on the BM02-D2AM beamline of the European Synchrotron Radiation Facility (ESRF, Grenoble, France). The NPs were placed between Kapton tapes on a home-made sample holder. The incident photon energy was set to 10.5 keV, and the beam diameter was on the order of 100 μm . The Si-based detector used was the ‘WOS’ (WAXS Open for SAXS), produced by IMXPAD [40]. The sample-to WOS detector distance was set to 12.0 cm. The scattering vector q ($q = 4\pi \sin \theta/\lambda$, where θ is the half of the scattering angle and λ is the incident wavelength) was calibrated using a chromium oxide standard (Cr_2O_3). The data acquisition time for each pattern was 100 s. Two dimensional data were corrected by considering the detector distortion, and the flat field response of the detector. The scattering diagrams $I(q)$ vs q (\AA^{-1}) were corrected by subtracting the signal of the empty cell with Kapton tape. The crystallite size was estimated from line broadening of the most intense diffraction peak ((311) reflection at $q \sim 2.49 \text{\AA}^{-1}$ ($2\theta \sim 35.5^\circ$)) by Scherrer’s equation (Equation 1).

$$D_{\text{WAXS}} = \frac{k \cdot \lambda}{\beta \cos \theta} \quad \text{Eq. 1}$$

where k is a constant ($k = 0.9$ for spheres), λ is the wavelength of $\text{Cu-K}_{\alpha 1}$ radiation ($\lambda = 1.5406 \text{\AA}$), β is the full width at half-maximum and θ is the Bragg angle. (The data were properly treated using the λ of $\text{Cu-K}_{\alpha 1}$ radiation to be comparable with the standard pattern (JCPDS card n $^\circ$ 88-0315)).

2.3.5.3. Small-angle X-ray scattering. Synchrotron SAXS was used to characterize the morphology of Fe_3O_4 and $\text{Fe}_3\text{O}_4\text{:COS}_{\text{DP/DA}}$ NPs in ultrapure water. The suspensions were prepared with concentration $\cong 0.1 \text{ g}\cdot\text{L}^{-1}$ of NPs in glass tubes (Deutero GmbH, ref. 600020-200, external diameter: 3 mm, length: 60 mm, width: 0.2 mm). The measurements were carried out at the European Synchrotron Radiation Facility (Grenoble, France) on BM2-D2AM beamline with the following settings: $E = 18 \text{ keV}$ ($\lambda = 0.6888 \text{\AA}$), sample-to-detector distance = 1.45 m. The detector used was the D5 IMXPAD solid state detector [40]. The image data treatments took into account the flat field response and blind zones between the detection modules. The collected scattering data were calibrated using silver behenate. The scattering diagrams $I(q)$ vs q (\AA^{-1}) were obtained by azimuthally averaging the corrected images, after the subtraction of the signals of the solvent and the empty cell.

2.3.6 Transmission Electron Microscopy (TEM). The morphology, particle size and microstructure characterizations were performed using the Transmission Electron Microscopes Philips CM120 and JEOL 2100F. Nanoparticle suspensions were prepared in deionized water and submitted to ultrasonic bath for 10 min, then dropped in the grid and the solvent dried at room temperature. It was possible to measure the size of a representative number of particles (minimum of 250 NPs) from image treatment using the software ImageJ

(<https://imagej.nih.gov/ij/>), even though the NPs are partially superimposed resulting in uncertainty in the apparent diameter.

2.3.7. Vibrating Sample Magnetometer (VSM). The magnetic curves (hysteresis loops) were determined, at room temperature, with a custom-made vibrating sample magnetometer under applied magnetic fields up to 15 kOe [41].

2.3.8 In vitro cytotoxicity analysis of COS, Fe₃O₄ and Fe₃O₄:COS. First, canine dermal fibroblasts were isolated from three healthy Beagle dogs owned by Institut Claude Bourgelat (VetAgro Sup - Campus Vétérinaire de Lyon, Marcy l'Etoile, France) in accordance with the VetAgro Sup animal ethics committee. Skin biopsy specimens were collected on dorsal surface of dogs after local anesthesia (lidocaine, Xylovet, Ceva, Libourne, France) and using a 6 skin biopsies punch under sterile conditions. Skin biopsies were cut into small fragments and digested with 0.25% trypsin/EDTA (Eurobio, Courtaboeuf, France) for 15 min at 37 °C. After digestion, the skin fragments were washed with PBS. Dermal fibroblast cultures were established by explant culture in 25 cm² flasks (Falcon, VWR international, Strasbourg, France) containing Dulbecco's Modified Eagle's Medium (DMEM, Eurobio, Courtaboeuf, France) supplemented with 20% fetal calf serum, 2 mM L-glutamine and 2% penicillin/streptomycin/amphotericin B (Eurobio, Courtaboeuf, France) at 37 °C in humidified atmosphere with 5% CO₂. After 4 days, fibroblasts started to grow out and fragments were removed. After 10 days, cells reached confluence and were sub-cultured after 0.25% trypsin/EDTA treatment in 75 cm² flasks (Falcon, VWR international, Strasbourg, France). Culture medium was changed twice a week. Cells were used between 3 and 10 amplification passages. In sequence, cell viability was investigated in accordance with the international standard operation procedure "Tests for in vitro cytotoxicity" ISO 10993-5. Cell cytotoxicity was assessed by the CCK-8 assay (Sigma Aldrich, Saint Quentin Fallavier, France) according to the manufacturer's instructions. Canine fibroblasts were seeded at a density of 1.0x10⁴ cells/well (2.6x10⁴ cells/cm²) in 96-well plate at 37 °C in humidified atmosphere with 5% CO₂. After 2 days of culture, the medium was replaced with fresh medium containing COS_{DP/DA} (DP/DA of 10/53, 24/24, 24/47, and 45/47) or NPs (Fe₃O₄, Fe₃O₄:COS_{10/53}, Fe₃O₄:COS_{24/24}, Fe₃O₄:COS_{24/47} and Fe₃O₄:COS_{45/47}). Two ranges of concentration, (0 [control], 60, 125, 250, 500 and 1000 µg/mL and 0 [control], 100, 500, 1000, 5000 and 10000 µg/mL) were used for NPs and COS_{DP/DA}, respectively. Two exposure times (24 h and 48 h) were tested in all cases. After 24 h or 48 h of incubation, 10 µL CCK8 were added into each well and incubated at 37 °C for 2 h. The absorbance was measured at 450 nm using a microplate reader (MultiSkan, Thermofisher). Cell viability was determined as the ratio of the optical density (OD) of exposed cells to the OD of the untreated cells. For each concentration of COS or NPs, mean values of the mean absorbance rates from eight wells were calculated. All experiments were performed in triplicate using fibroblasts obtained from three different dogs. Results were expressed as mean ± standard deviation. Differences among the different COS_{DP/DA} or among Fe₃O₄, Fe₃O₄:COS_{DP/DA} were analyzed at each concentration using an unpaired Student's t test. Graphs and statistical analyses were performed using GraphPad Prism version 7 software. p-values ≤ 0.05 were considered significant.

3. Results and Discussion

In order to characterize the reacylated COS_{DP/DA}, infrared spectra were recorded and are shown in Figure 1 (a). The most characteristic absorption bands from COS_{DP/DA} are [42-45]: a) axial stretching of O-H and N-H bonds in the range of 3600 to 3000 cm⁻¹; b) axial stretching of the -C-H for -CH₂ (2930 cm⁻¹) and -CH₃ (2875 cm⁻¹) bonds; c) axial stretching of C=O bonds at 1655 cm⁻¹ for acetamide groups (amide I); d) angular deformation of N-H bonds for amine groups (-NH₂) at 1558 cm⁻¹; e) absorption bands at 1417 cm⁻¹ and 1377 cm⁻¹ associated to the coupling of C-H angular deformation and C-N axial stretching; (f) absorption bands corresponding to the polysaccharide skeleton, including the C-O and C-O-C stretching vibrations of the glycosidic bonds in the range 1153 to 897 cm⁻¹. As can be seen in the Figure 1 (a), FTIR spectra of COS exhibit some differences in the 1680-1480 cm⁻¹ range due to different DAs. In this range, characteristic absorption bands related to the carbonyl group (C=O) of the secondary amide group (1641 cm⁻¹) and the absorption band of the primary amino group -NH₂ (1590 cm⁻¹), can be observed. As expected, the relative intensity of the absorption band of the amino group at 1590 cm⁻¹ is more intense for COS with DA ≅ 50 % than for COS with DA ≅ 24 % [45, 46].

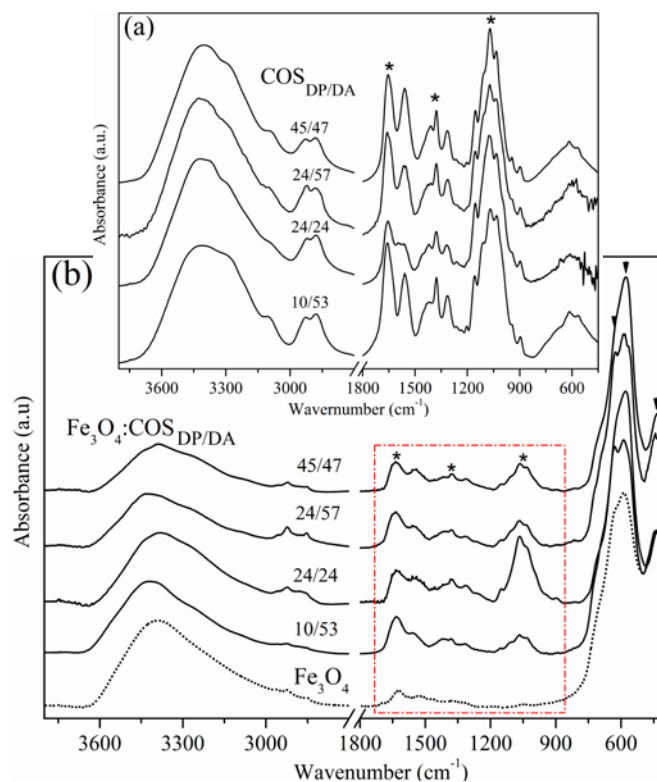


Figure 1 – (a) Normalized infrared spectra of the chito-oligosaccharides, $\text{COS}_{\text{DP/DA}}$. (b) Normalized infrared spectra for Fe_3O_4 , $\text{Fe}_3\text{O}_4:\text{COS}_{\text{DP/DA}}$. *Indication of COS absorption bands that can be clearly identified on the $\text{Fe}_3\text{O}_4:\text{COS}_{\text{DP/DA}}$ spectra. ▼ Characteristics absorption bands for the Fe-O stretching.

Figure 1 (b) shows the FT-IR spectra of Fe_3O_4 and the different $\text{Fe}_3\text{O}_4:\text{COS}_{\text{DP/DA}}$. The characteristic absorption bands of the Fe-O bond of bulk magnetite was previously reported to be at 570 and 375 cm^{-1} [47]. However, in Figure 1(B) these two absorption bands shift to higher wavenumbers close to 600 and 440 cm^{-1} respectively, and the band near 600 cm^{-1} is divided into two absorption bands at 622 and 590 cm^{-1} , well defined for the $\text{COS}_{10/53}$ and $\text{COS}_{24/47}$ samples. In the case of the two other COS, $\text{COS}_{24/24}$ and $\text{COS}_{45/47}$, a shoulder can be observed in the spectra at 622 cm^{-1} . The main effect of the small size of NPs is the breaking/distortion of a large number of Fe-O bonds in the vicinity of the surface, resulting in the rearrangement of delocalized electrons on the particle surface. As a result, the apparent surface bond force constant increases as Fe_3O_4 is reduced to nanoscale, so that the absorption bands of infrared spectra shift to higher wavenumbers. In addition, the split of the bands is attributed to a split of the energy levels of the quantized Fe_3O_4 NPs [48]. In comparison with the Fe_3O_4 FTIR spectrum, the spectra of the different $\text{Fe}_3\text{O}_4:\text{COS}_{\text{DP/DA}}$ also exhibited the typical absorption bands of magnetite at 622, 590 and 440 cm^{-1} , in addition to absorption bands characterizing the presence of COS. As for example, the absorption bands at 1655 cm^{-1} from the axial stretching of C=O bonds (amide I), at 1070 cm^{-1} attributed to stretching of C-O-C and the coupling of absorption bands at 1417 cm^{-1} (angular deformation of -C-H) and at 1377 cm^{-1} (axial stretching of -C-N) can be observed. It can be noticed that for the sample $\text{Fe}_3\text{O}_4:\text{COS}_{24/24}$, these absorption bands are slightly more intense (see Figure 1 (b)), suggesting a higher quantity of COS. As in fact confirmed by other analyses presented below. As can be seen in the spectra of different $\text{Fe}_3\text{O}_4:\text{COS}_{\text{DP/DA}}$, the presence of the characteristic absorption bands of COS indicates that the magnetite NPs were successfully coated by the studied $\text{COS}_{\text{DP/DA}}$.

For estimating the proportion of organic and inorganic phases in the $\text{Fe}_3\text{O}_4:\text{COS}$ NPs, thermal characterizations were performed in the temperature range of 30 to 700 $^{\circ}\text{C}$. In the thermograms showed in Figure 2, the mass losses, below 150 $^{\circ}\text{C}$, are due to water desorption. Pure $\text{COS}_{\text{DP/DA}}$ had more adsorbed water (maximum $\sim 8.64\%$ for the $\text{COS}_{24/24}$) than the other samples (Fe_3O_4 NPs and COS-coated NPs, maximum of $\sim 3.44\%$ for $\text{Fe}_3\text{O}_4:\text{COS}_{24/24}$). Pure $\text{COS}_{\text{DP/DA}}$ started to be degraded at 200 $^{\circ}\text{C}$ and were completely degraded at 600 $^{\circ}\text{C}$, as shown in Figure 2 (a). The degradation of COS in the presence of Fe_3O_4 NPs starts at lower temperature in comparison with pure COS, *i.e.* at 160 $^{\circ}\text{C}$, and finishes around 400 $^{\circ}\text{C}$ (see Figure 2 (b)), for the different

COS_{DP/DA}. This degradation process at lower temperature is an indicative of COS-Fe₃O₄ interactions, resulting from a coating of magnetite NPs by COS. In the case of Fe₃O₄ NPs and coated Fe₃O₄ NPs, it can be suggested that the formation of α -Fe₂O₃ (hematite) occurred at high temperature, since the TGA analyses were performed under dry air [49, 50]. Moreover, air atmosphere was used in the TGA analyses to induce the complete degradation of COS which, when performed under inert atmosphere, always leaves residual mass. Then, for the calculation of the COS mass on the initial COS-coated NPs, full conversion of Fe₃O₄ to α -Fe₂O₃ was hypothesized as final inorganic product [49]. This supposition was grounded by the fact that the initial products show a black color (characteristic for magnetite) whereas at the end of TGA experiment the final powder showed a red color without magnetic properties (characteristic for hematite), which is an indication of α -Fe₂O₃ formation (see SM-Figure 4). Then, the heat-treated sample was analyzed by XRD evidencing the characteristic pattern of the hematite, as shown in the supporting material (SM-Figure 5). Therefore, the initial mass of magnetite was calculated and the mass percentage of COS, in Fe₃O₄:COS_{DP/DA} samples, was deduced and reported in Table 2. These estimations are in good agreement with the results of FTIR analysis, which showed more intense absorption bands characteristics of COS for the Fe₃O₄:COS_{24/24} sample.

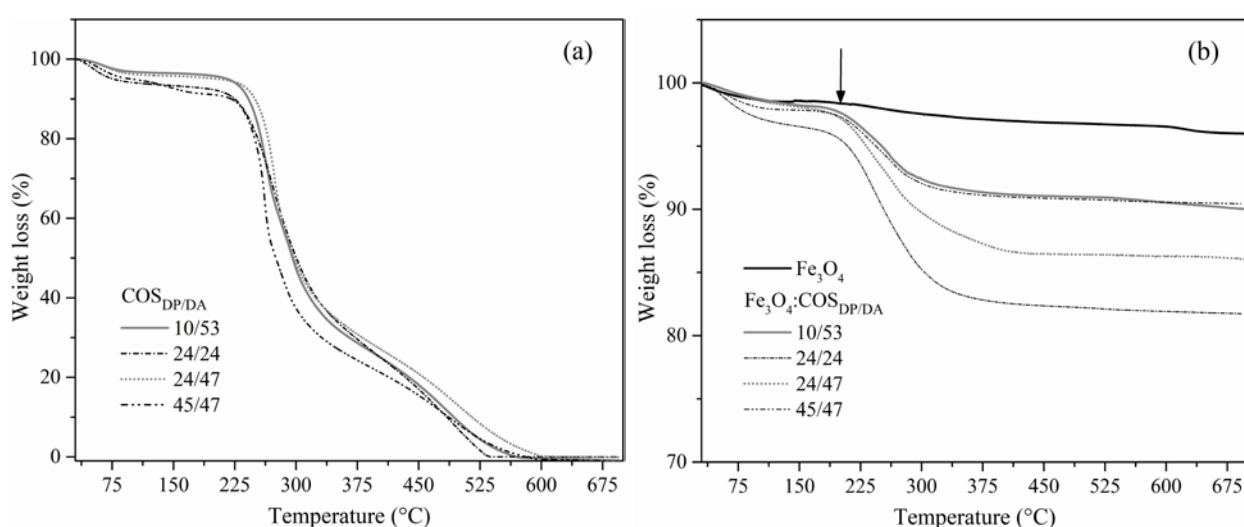


Figure 2 - (a) Thermogravimetric curves for COS_{DP/DA}; (b) Thermogravimetric curves of Fe₃O₄ and Fe₃O₄:COS_{DP/DA} nanoparticles.

The XRD patterns for Fe₃O₄ and Fe₃O₄:COS_{DP/DA} NPs are shown in Figure 3. The XRD patterns of all synthesized NPs (Figure 3 (a)) show a complete agreement with the standard pattern for magnetite (JCPDS card n° 88-0315) with the characteristic diffraction peaks at 18.15° (111), 30.11° (220), 35.54° (311), 37.16° (222), 43.28° (400), 53.77° (422), 57.27° (511) and 62.95°(440). The diffraction peak positions indicate that all samples can be indexed with the expected cubic spinel structure ($Fd\bar{3}m$ space group) of the Fe₃O₄ compound. However, the formation of NPs in the presence of COS_{DP/DA} impacts the XRD results, since thinner peaks could be observed for Fe₃O₄:COS_{DP/DA} NPs (see Figure 3 (b)). In fact, it was observed a decrease of the peak width of the most intense peak at $2\theta = 35.5^\circ$, when the Fe₃O₄ was synthesized in the presence of COS_{10/53} and COS_{45/47}. This effect was slightly more pronounced using the COS_{DP/DA} with DP/DA of 45/47, as shown in Figure 3 (b), reflecting an increase of the crystallite size (see Table 2). WAXS experiments are consistent with XRD and the peaks associated with the (111), (220), (311) and (400) reflections could also be observed at the WAXS spectra that are shown in the Supporting Material (SM-Figure 6). Similarly to XRD, the WAXS results also show thinner diffraction peaks when the Fe₃O₄ NPs were formed in the presence of COS_{DP/DA}, suggesting a longer range ordering of the Fe₃O₄ crystalline structure in comparison with Fe₃O₄ prepared without COS. The apparent crystallite sizes of the synthesized Fe₃O₄ and the different Fe₃O₄:COS_{DP/DA} NPs were calculated from the WAXS patterns using the Scherrer equation (Equation 1) on the strongest peak (311). The estimated crystallite sizes are shown in the Table 2.

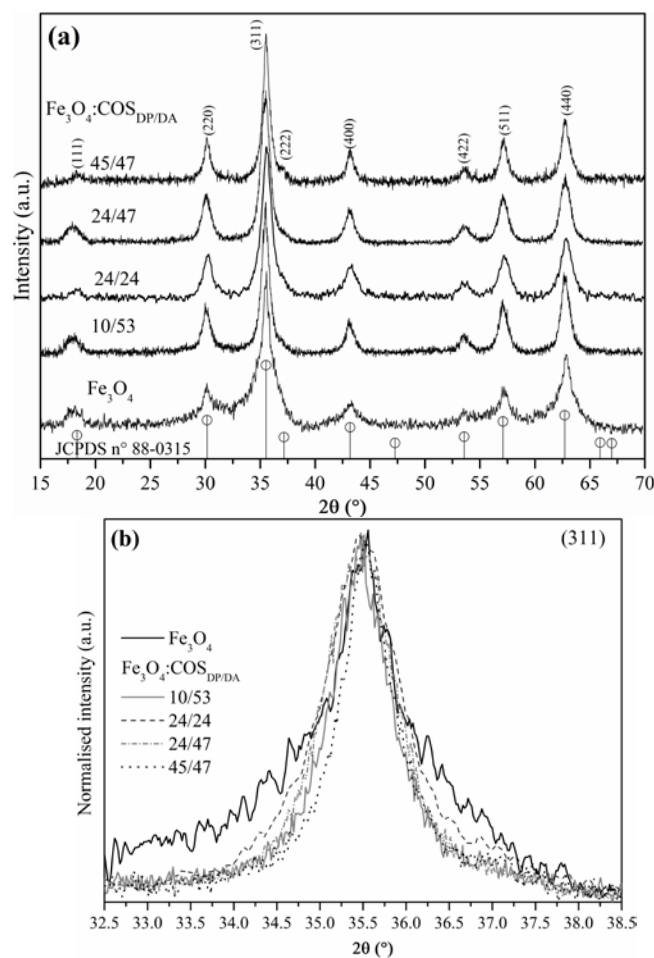


Figure 3 - (a) X-ray diffraction patterns for Fe_3O_4 and $\text{Fe}_3\text{O}_4:\text{COS}_{\text{DP/DA}}$ nanoparticles and comparison with JCPDS n° 88-0315 card. (b) Enlarged view showing the normalized intensities of the (311) reflection peak for Fe_3O_4 and $\text{Fe}_3\text{O}_4:\text{COS}_{\text{DP/DA}}$ nanoparticles.

Figure 4 shows SAXS scattering profiles for Fe_3O_4 NPs and several $\text{Fe}_3\text{O}_4:\text{COS}_{\text{DP/DA}}$ NPs in water. Due to the large contrast in scattering length density among Fe_3O_4 , COS and water, the signal from Fe_3O_4 dominates largely the signal, and the COS structure cannot be determined by this method.

All the curves consist of a “knee-like” Guinier regime in between two power-law regimes. This suggests, as confirmed by TEM images (see below), that the NPs form aggregates. The profiles show a power-law variation $I(q) \propto q^{-\alpha}$ with $\alpha \approx 3$ in the low q region (for $q < 0.02 \text{ \AA}^{-1}$). This variation is an indicative of the strong roughness of the aggregates. In the case of Fe_3O_4 and $\text{Fe}_3\text{O}_4:\text{COS}_{45/47}$ NPs, although slight slope changes can be observed, no clear Guinier regime can be identified, which suggests that the particle size is broadly distributed, and/or that the roughness of the particles is similar to that of the aggregates.

In the case of the $\text{Fe}_3\text{O}_4:\text{COS}_{10/53}$, $\text{Fe}_3\text{O}_4:\text{COS}_{24/24}$ and $\text{Fe}_3\text{O}_4:\text{COS}_{24/47}$ NPs, the Guinier regime is visible and can be fitted to obtain the average radius of gyration, R_g , of these NPs (the best fits are presented in Figures. 4 (b), (c) and (d) for $\text{Fe}_3\text{O}_4:\text{COS}_{10/53}$, $\text{Fe}_3\text{O}_4:\text{COS}_{24/24}$ and $\text{Fe}_3\text{O}_4:\text{COS}_{24/47}$ NPs, respectively). The obtained R_g can be used to determine the average equivalent diameters d_e ($d_e = 2 (5/3)^{0.5} R_g$ for spheres) which are reported in Table 2. At higher q values ($q > 0.13 \text{ \AA}^{-1}$), a second power-law regime can be extracted. It has to be noted that for the high DA ≈ 50 systems of $\text{Fe}_3\text{O}_4:\text{COS}_{\text{DP/DA}}$, the variation $I(q) \propto q^{-\alpha}$ is obtained with $\alpha \approx 4$, which suggests that the surface of the particles is sharp and smooth, while for the intermediate DA ≈ 24 systems of $\text{Fe}_3\text{O}_4:\text{COS}_{\text{DP/DA}}$, α is inferior to 4, suggesting that the obtained particles have rougher surfaces.

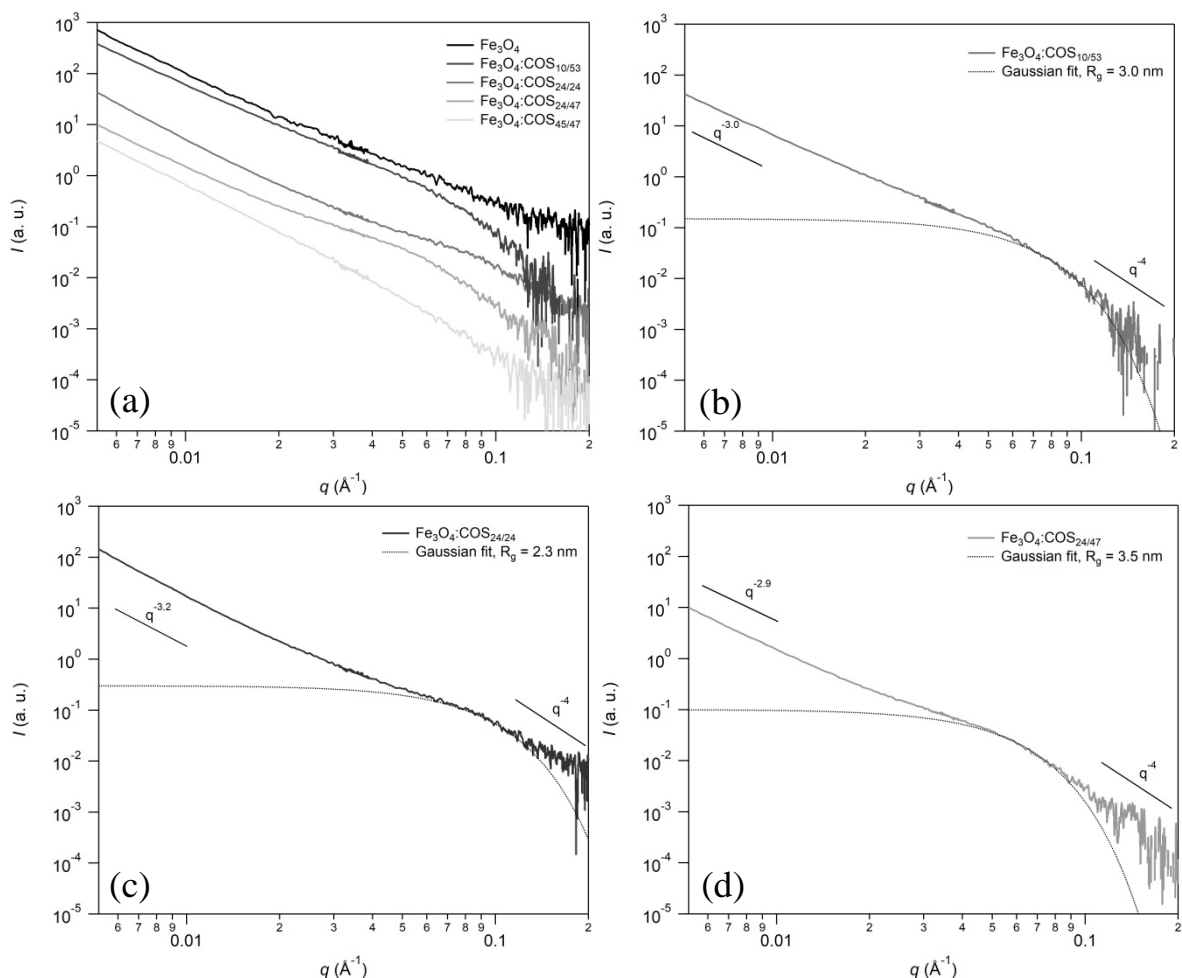


Figure 4 – (a) SAXS profiles obtained for Fe_3O_4 and $\text{Fe}_3\text{O}_4:\text{COS}_{\text{DP/DA}}$ nanoparticles dispersed in water. SAXS profile analyses for (b) $\text{Fe}_3\text{O}_4:\text{COS}_{10/53}$, (c) $\text{Fe}_3\text{O}_4:\text{COS}_{24/24}$, and (d) $\text{Fe}_3\text{O}_4:\text{COS}_{24/47}$ nanoparticles dispersed in water. The Guinier model which best fits the “knee-like” part of the curves for the determination of the gyration radius R_g of the nanoparticles was used.

TEM investigations were used to deduce the size and the morphology of the NPs. Figure 5 shows TEM images of Fe_3O_4 and $\text{Fe}_3\text{O}_4:\text{COS}_{\text{DP/DA}}$ NPs and their size histograms fitted by using log-normal distribution functions. As the particles displayed similar contrast and were not observed distinct artifacts materials on the images, it can be suggested that the COS (organic phase) formed a thin shell over the inorganic magnetite phase. Thus, the $\text{Fe}_3\text{O}_4:\text{COS}$ NPs should consist in a crystalline Fe_3O_4 core covered by a COS organic shell. The average particle sizes can be observed in the histograms in Figure 5 (c), (f), (i), (l) and (o). Fe_3O_4 NPs exhibited a nearly spherical shape with an average diameter of 6.5 ± 2.5 nm. As a result of suspension drying, aggregates were present and made difficult the estimation of individual particles diameter. The obtained Fe_3O_4 NPs coated by the different $\text{COS}_{\text{DP/DA}}$ also exhibit a spherical morphology, but with lower size dispersity in comparison with Fe_3O_4 NPs. Such TEM results are a strong indication that COS might act as steric stabilization agent and prevent aggregation of the Fe_3O_4 NPs, also acting in the nucleation process by helping to narrow the size distribution. This phenomenon was in fact more pronounced for the COS with smaller DP. The particles prepared in the presence of $\text{COS}_{45/47}$ presented the highest size dispersity in comparison with the other NPs coated by $\text{COS}_{\text{DP/DA}}$ analyzed in this work and also the nanoparticles biggest average diameter, 7.4 ± 2.2 nm. This may result in a lower ability of this COS to separate the ions iron during the nucleation process by complexation and steric hindrance. HR-TEM images of the $\text{Fe}_3\text{O}_4:\text{COS}_{45/47}$ nanoparticles are shown in the Supporting Material, SM-Figure 7.

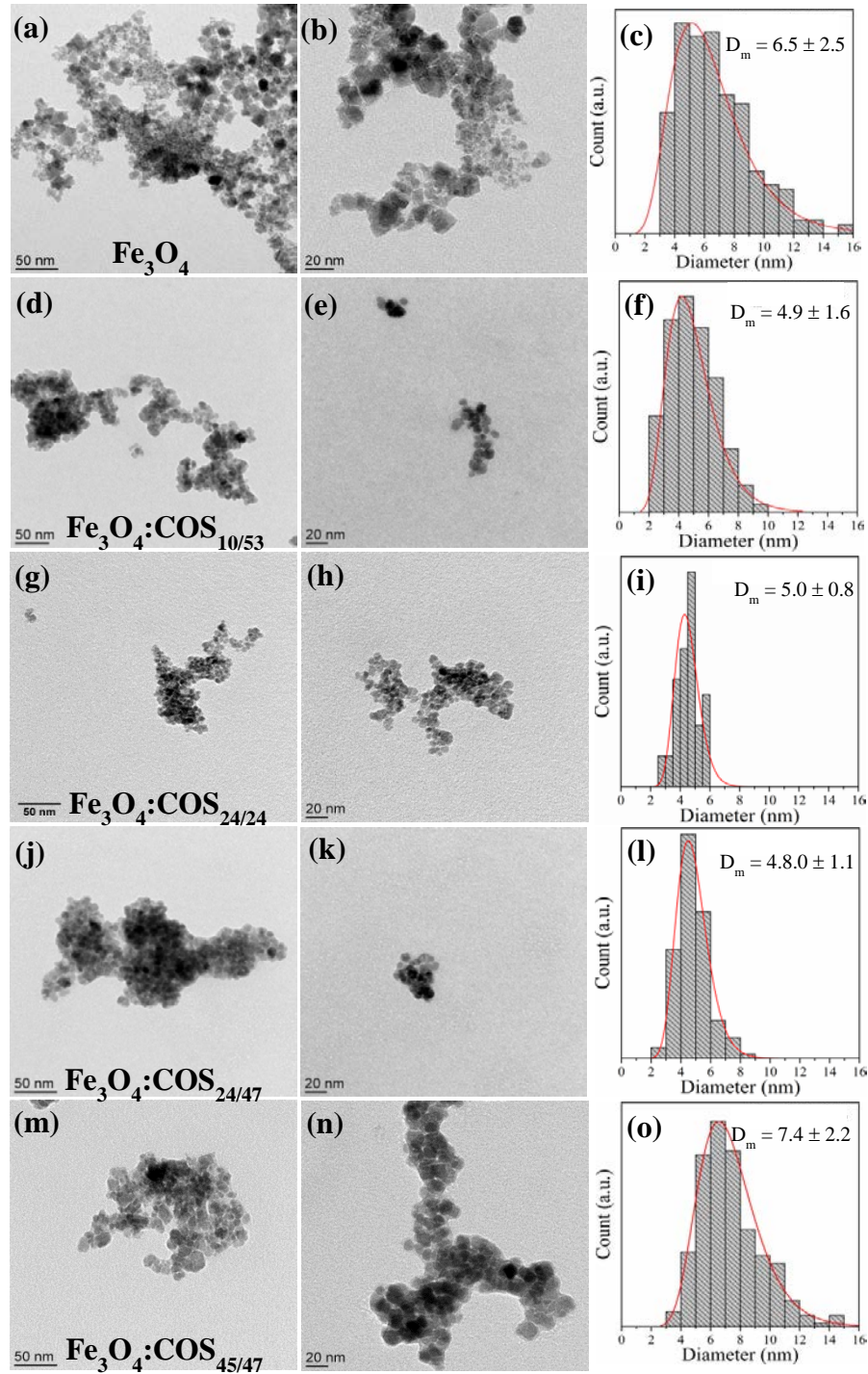


Figure 5 – TEM images and histograms showing particle size distribution profiles (the straight lines are lognormal fittings) for Fe_3O_4 (a, b and c), $\text{Fe}_3\text{O}_4\text{:COS}_{10/53}$ (d, e and f), $\text{Fe}_3\text{O}_4\text{:COS}_{24/24}$ (g, h and i), $\text{Fe}_3\text{O}_4\text{:COS}_{24/47}$ (j, k and l) and $\text{Fe}_3\text{O}_4\text{:COS}_{45/47}$ (m, n and o).

In order to study the magnetic behavior of Fe_3O_4 and $\text{Fe}_3\text{O}_4\text{:COS}_{\text{DP/DA}}$ NPs magnetization measurements were performed at room temperature. According to Figure 6, the saturation magnetizations (M_s) obtained for synthesized magnetite NPs are lower than that reported for multi-domain bulk magnetite ($\cong 90$ emu/g) [51]. The values of M_s are listed in Table 2. Figure 6 (b) shows the details of hysteresis curves of each nanoparticle analyzed in a wide external magnetic field range. In general, Fe_3O_4 NPs present a magnetization slightly lower than that of Fe_3O_4 NPs coated by COS. It is reported in the literature that saturation magnetization of ferrite NPs sharply decreases with decreasing of the particle size due to finite size effects (*i.e.* surface spin contributions) and surface defects (*i.e.*, breaking of the surface crystal symmetry) [52, 53]. In fact, defects in the particles

surface contribute to decrease the coercivity of NPs systems and increase the magnetic anisotropy [54]. Furthermore, an organic layer on the particles surface can also contribute to an apparent decrease in the *specific* M_s values, since it is proportional to the mass used in the tests [55]. As the mass of COS on the NPs was determined by TGA, the M_s could be properly corrected by considering the inorganic mass for determining the M_s only for the magnetic core of the particle. The M_s values for $\text{Fe}_3\text{O}_4:\text{COS}_{10/53}$, $\text{Fe}_3\text{O}_4:\text{COS}_{24/24}$, $\text{Fe}_3\text{O}_4:\text{COS}_{24/47}$ and $\text{Fe}_3\text{O}_4:\text{COS}_{45/47}$ NPs are listed in the Table 2. This means a substantial increase of saturation magnetization with percentages between 18 and 22% in comparison with the pure Fe_3O_4 . It is worth mentioning that discrepancies in the saturation magnetization reported by different authors may be explained by variations in the methods employed to synthesize magnetite, which can generate different particle sizes, surfaces, crystalline defects and chemical compositions [34, 35, 56]. Additionally, Fe_3O_4 NPs can undergo an oxidative process and thus their external part (surface) can lose their magnetic properties. As the $\text{Fe}_3\text{O}_4:\text{COS}$ NPs have COS on their surface, COS act as a protective layer preventing the oxidation of the core (Fe_3O_4) and increasing the surface structural organization. In fact, the presence of COS may favor the synthesis process of magnetite, possibly through the complexation between the iron ions and the amino groups of COS. This approach results in a more ordered crystalline structure, as could be evidenced by X-ray diffraction analysis, also leading to higher saturation magnetizations in comparison with the pure Fe_3O_4 NPs. These significant increases of saturation magnetization (between 18 and 22%) probably will be able to induce a better performance for these NPs, for example, in imaging tests (MRI) (better image contrast) or hyperthermia (providing higher heating at lower energy transfer rates).

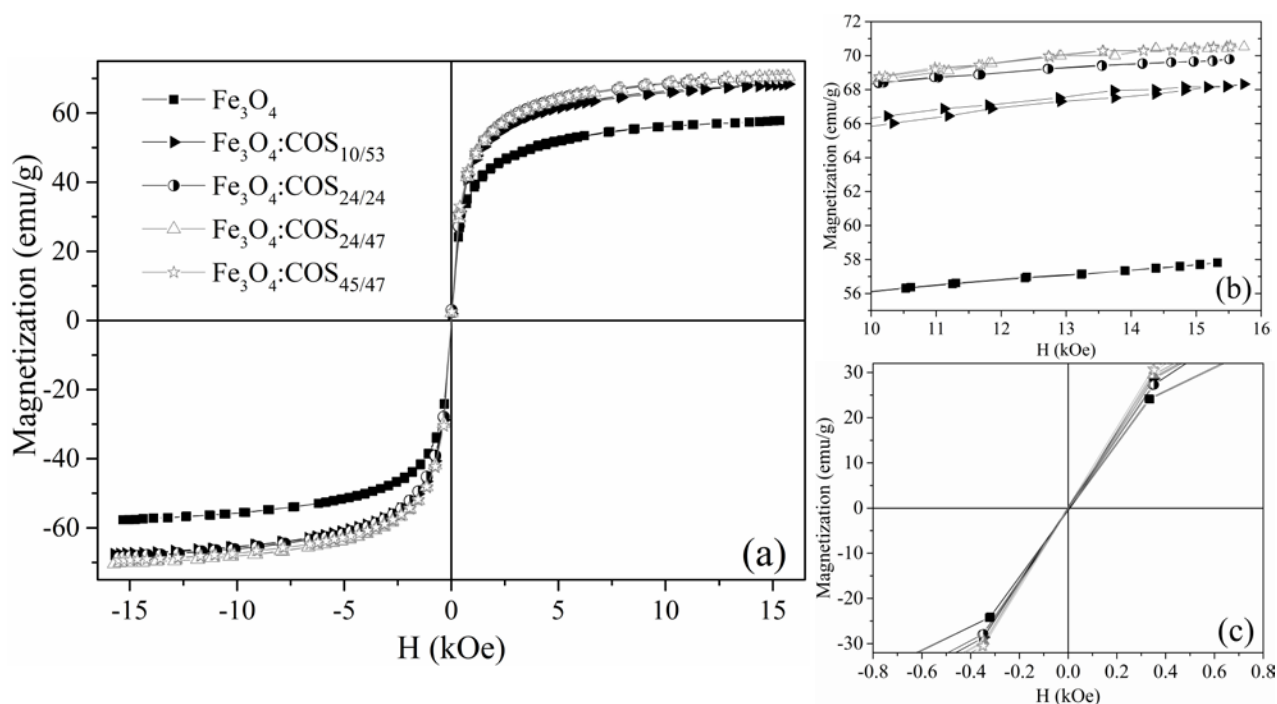


Figure 6 - (a) $M \times H$ curves, at room temperature, for Fe_3O_4 and $\text{Fe}_3\text{O}_4:\text{COS}_{\text{DP/DA}}$ nanoparticles; (b) Enlarged view of the magnetization (high magnetic field region) showing the difference in magnetization saturation among the processed nanoparticles. (c) Enlarged view of the magnetization curves (for magnetic fields nearby zero) emphasizing the superparamagnetic-like behavior (visually null coercivity) of the processed nanoparticles.

As observed in Figure 6 (a), the magnetization curves measured for Fe_3O_4 and $\text{Fe}_3\text{O}_4:\text{COS}_{\text{DP/DA}}$ NPs showed fully reversible hysteresis loops. In these hysteresis curves, almost zero coercivity (H_c) and zero remanence magnetization (M_r) are observed (see Figure 6 (c)). These characteristics indicate that the synthesized MNPs exhibit superparamagnetic-like behavior at room temperature, a feature that is expected for nanometer-scaled particle sizes [1, 57]. In fact, the superparamagnetic behavior can be very useful for medical purposes as already mentioned (*i.e.* for the manipulation of the MNPs in a biological medium with an external magnetic field).

As often described in literature, Fe_3O_4 NPs can be considered magnetic single domains for sizes lower than ~ 20 nm [58]. The magnetic response of these single domains can be described by using a modified Langevin function

[59]. Then, the total magnetic contribution of a collection of NPs with a size distribution can be modeled using a normalized lognormal distribution of the magnetic moments, as proposed by Cótica *et al.* [60]:

$$M(H, T) = \int \mu L\left(\frac{\mu H}{k_B T}\right) f(\mu) d\mu \quad \text{Eq. 2}$$

where μ is the particle magnetic moment, H is the amplitude of the applied magnetic field, and k_B is the Boltzmann constant. The relation between the volume distribution of particles, V , and the magnetic moment distribution of these particles, μ , can be further written considering that the magnetic interactions always increase with the nanoparticle size growth. Thus, applying the relationship: $f(V)dV=(\mu/M_s)f(\mu)d\mu$, and considering that the particles are spherical, the mean particle volume and diameter can be obtained by calculating the magnetic moment per Fe_3O_4 unit cell by using structural considerations [58, 59]. The mean particle diameters calculated from this equation are shown in Table 2. The Equation 2 was used to fit the first part of the hysteresis loops in the experimental $M \times H$ data (for each sample) and the results of these fits can be observed in Figure 7.

Table 2 - Structural and microstructural features for the processed samples: mass percentage of $\text{COS}_{\text{DP/DA}}$ in the $\text{Fe}_3\text{O}_4:\text{COS}_{\text{DP/DA}}$ samples; crystallite sizes determined from WAXS results applying Scherrer equation (Equation 1); average equivalent diameter from the SAXS spectra (d_e); saturation magnetization (M_s); and mean particle diameters determined from the magnetization curves ($M \times H$) at room temperature:

Samples	COS mass	Apparent Scherrer Crystallite size	d_e	M_s	D_m
	TGA (%)	WAXS (nm)	SAXS (nm)	(emu/g)	$M \times H$ (nm)
Fe_3O_4	-	9.4	-	57.8	8.8
$\text{Fe}_3\text{O}_4:\text{COS}_{10/53}$	11.3	10.7	7.8	68.3	8.6
$\text{Fe}_3\text{O}_4:\text{COS}_{24/24}$	17.7	8.2	5.9	69.9	8.3
$\text{Fe}_3\text{O}_4:\text{COS}_{24/47}$	15.1	8.6	9.0	70.4	8.6
$\text{Fe}_3\text{O}_4:\text{COS}_{45/47}$	10.5	11.7	-	70.5	8.7

The theoretical model reproduces accurately the experimental results, supporting the superparamagnetic-like behavior for the studied samples. It is worth nothing that the fit is composed of two contributions, namely the Langevin function term, *i.e.*, a non-linear contribution of $M(H)$, and $M = \chi H$, for the linear contribution. The linear contribution characterizes a paramagnetic response that can be associated to the defects on the surface of the NPs that usually become more pronounced as the size of these particles becomes smaller [55]. As observed in Figure 7, the contribution of the surface defects is smaller in that NPs coated by chitosan than for Fe_3O_4 alone. It shows that the presence of COS on the surface of the Fe_3O_4 NPs reduces the surface spin and surface structural disorders, promoting the formation of the Fe_3O_4 crystalline structure in almost all particle volume, as previously mentioned. Furthermore, COS can act as a protection to the Fe_3O_4 core, preventing the formation of Fe_2O_3 by oxidation, which usually reduces the net magnetization. As shown in Figure 6, all the NPs showed similar $M \times H$ curves and consequently only a slight difference could be noted among their diameter values (D_m) (see Table 2).

In order to validate the potential for biomedical applications of the NPs synthesized by the COS-assisted precipitation process, the cytotoxicity of $\text{COS}_{\text{DP/DA}}$ and MNPs (Fe_3O_4 and $\text{Fe}_3\text{O}_4:\text{COS}_{\text{DP/DA}}$) have been assessed through CCK8 assay. This assay is based on the reduction of soluble tetrazolium salt to an orange-colored formazan (WST-8) through a cellular dehydrogenase. Therefore, the amount of WST-8 formazan is directly proportional to total cellular dehydrogenase expression and hence, to the number of viable cells [61]. The outcomes of these *in vitro* cytotoxicity studies have been achieved after 24 h and 48 h of incubation with various concentrations of COS or NPs as illustrated in Figures 8 and 9, respectively.

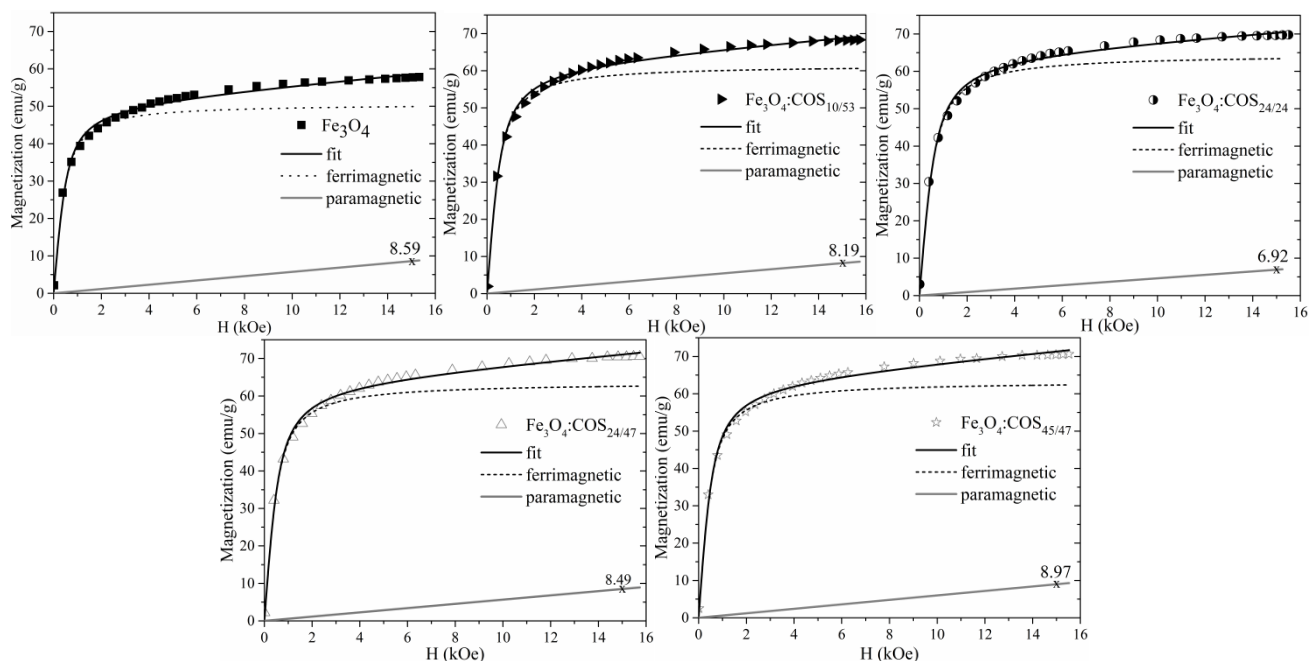


Figure 7 - First part of $M \times H$ curves for Fe_3O_4 , $\text{Fe}_3\text{O}_4:\text{COS}_{10/53}$, $\text{Fe}_3\text{O}_4:\text{COS}_{24/24}$, $\text{Fe}_3\text{O}_4:\text{COS}_{24/47}$, $\text{Fe}_3\text{O}_4:\text{COS}_{45/47}$ NPs (symbols). The continuous black lines are the best fit results using Langevin function (Equation 2). Black dashed and grey continuous lines show, respectively, the non-linear and linear contributions of the magnetization curves (continuous line – values specified at 15 kOe).

As shown in Figure 8, the different COS had generally a low impact on the cell viability even after 48 h of incubation. Some differences could be observed especially at higher concentrations after 24 h and 48 h of exposure. However, it can be noticed that the cell viability remained between 75 % and 90 % (in comparison with control cells) after 24 h and 48 h of exposure. According to the international standard operation procedure “Tests for in vitro cytotoxicity” ISO 10993-5, which sets a threshold of 70% of cell viability to evidence a toxic effect, the different COSs analyzed were not cytotoxic in the conditions of incubation (see dashed red horizontal lines in Figures 8 and 9).

Previous studies laid emphasis on the low cytotoxicity of COS on human and mouse fibroblast at 1 mg/mL [62]. For mouse fibroblasts L929 cell line, COS cytotoxicity was observed for concentrations higher than 5 mg/mL [63]. Lv *et al.* studied the introduction of COS in hydrogels based on carboxymethyl chitosan and alginate (COS with $M_n \sim 1000$ g/mol, DA < 10%, prepared by enzymolysis method). They observed that the presence of COS promoted the proliferation of human umbilical cord mesenchymal stem cells. In addition, the injectable hydrogels with COS remarkably accelerated the wound healing process in mouse skin defect model, induced anti-inflammatory effect with the absence of cytotoxicity [64]. Unfortunately, comparing literature data about COS cytotoxicity is still a difficult task due the diversity of COS molecular structures (chain size, DA and sequence of repeat units) and sometimes the lack of full characterization of COS.

Previous studies also have shown that the cytotoxicity of magnetite particle suspensions depend on the NPs concentration (in general 100 $\mu\text{g}/\text{mL}$) as well as the surface coating material [65-67]. The variation of cell viabilities of Fe_3O_4 and $\text{Fe}_3\text{O}_4:\text{COS}_{\text{DP}/\text{DA}}$ NPs for the incubation times of 24 and 48 h are shown in Figure 9. Each nanoparticle displays a dose effect. In the case of Fe_3O_4 NPs, a significant impact on primary canine fibroblasts viability was observed, with cell viability at 24 h increasing from 20% to 85% with concentrations varying from 1000 to 60 $\mu\text{g}/\text{mL}$. Similar results were obtained at 48 h and are consistent with previous works, showing the Fe_3O_4 NPs cytotoxicity on cell lines, as well as primary cells, above the concentration of 125 $\mu\text{g}/\text{mL}$ [68, 69].

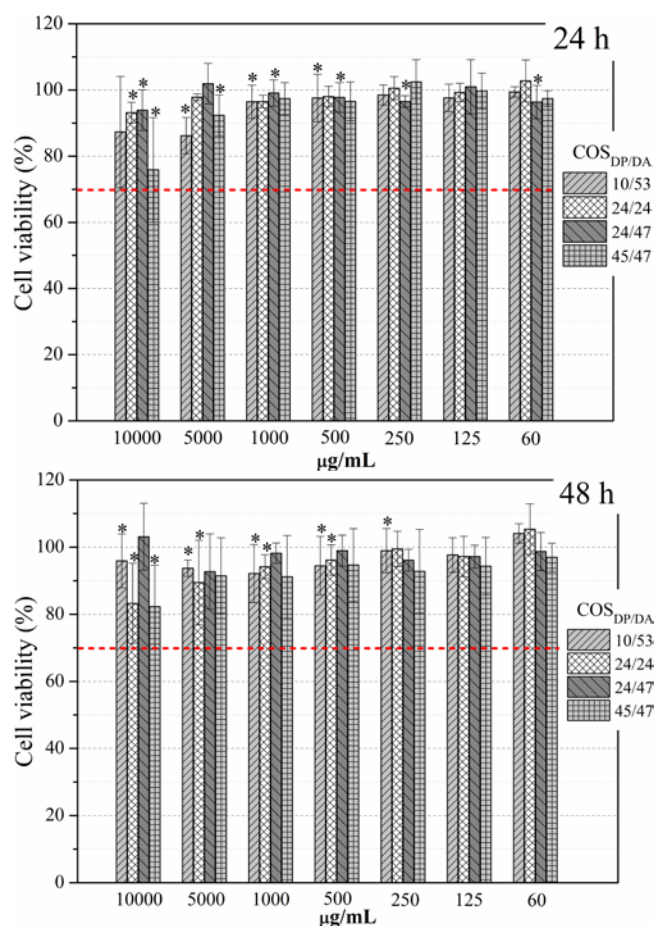


Figure 8 – Cell viability assay of COS with the different DP/DA against canine fibroblasts cells, at different COS concentrations (60 to 1000 $\mu\text{g/mL}$) at 24 h and 48 h. Data are mean \pm S.D. expressed as % of control response. *Statistically different from control cell monolayers, using $p < 0.05$. Red dashed line-threshold limited or cell viability (ISO 10993-5).

Figure 9 shows that the COS coating of Fe_3O_4 NPs strongly increases the cell viability with a concentration dependence. It is important to highlight the changing of the limit of cell viability for $\text{Fe}_3\text{O}_4\text{:COS}_{\text{DP/DA}}$ samples in comparison with pure Fe_3O_4 NPs. In fact, COS-coated Fe_3O_4 NPs exhibit a cell viability exceeding 70% for the concentration of 250 $\mu\text{g/mL}$, an enhancement of 100% in the NPs concentration, in comparison with uncoated Fe_3O_4 (cell viability limit at the concentration of 125 $\mu\text{g/mL}$). Coating Fe_3O_4 NPs with polymers is known to decrease their toxicity and our results confirm this general trend for COS coatings. In fact, Mahmoudi *et al.* showed on a mouse fibroblast cell line that uncoated particles induced a greater toxicity than the particles coated with the biocompatible polyvinyl alcohol (PVA) [70]. Shukla *et al.* demonstrated that COS coating on iron oxide NPs decrease cellular damage, ROS production, and the cytotoxic impact [33]. In addition, the Fe_3O_4 NPs coated by the $\text{COS}_{10/53}$ and $\text{COS}_{45/47}$ are slightly less cytotoxic for all concentrations and for both incubation times tested, followed by the $\text{Fe}_3\text{O}_4\text{:COS}_{24/47}$. Similar results were observed at 24 and 48 h. The three best results have in common a DA $\sim 50\%$, which corresponds to the COS with the higher water solubility. Thus, chain hydration could result in a more extended chain conformation and a thicker interfacial zone, inducing a stronger separation between the iron oxide core and the biological medium. However, it is necessary to perform further systematic analyses to strengthen the relations between $\text{Fe}_3\text{O}_4\text{:COS}$ cytotoxicity and the COS structure (chain size, DA and even the sequence of residues). For further application of COS coated Fe_3O_4 NPs, it is also necessary to analyze the cell uptake and determine the intracellular biodistribution and behavior of this type of NPs. Thus, Fe_3O_4 NPs coated by COS may be suitable as magnetic nanocarriers in biomedical applications such as targeted drug delivery, magnetic resonance imaging (MRI), marker cell tracking and magnetic hyperthermia.

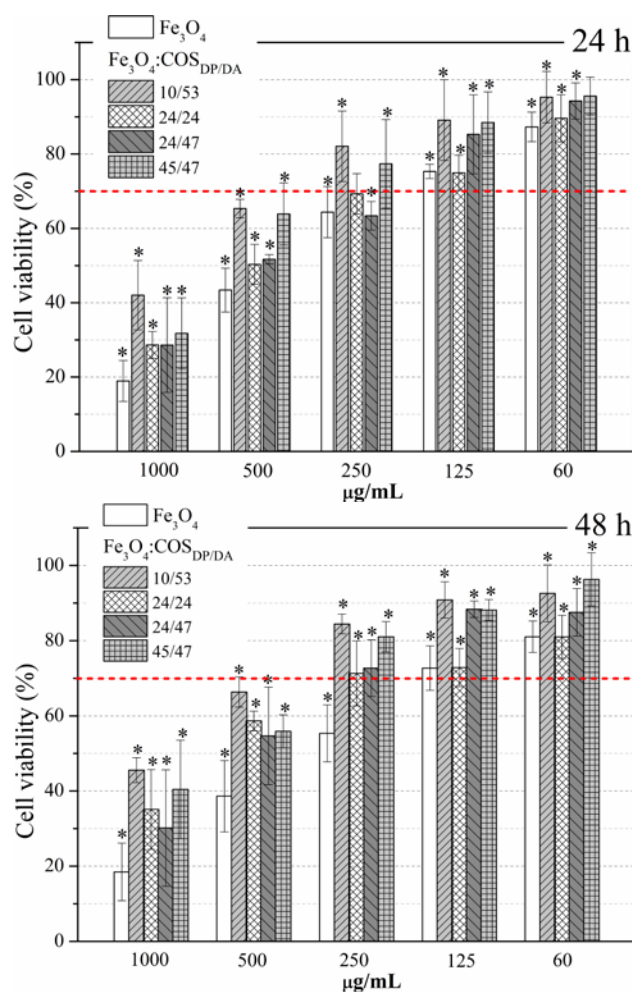


Figure 9 - Cell viability assay of Fe₃O₄ and Fe₃O₄:COS_{DP/DA} nanoparticles against canine fibroblasts cells, at different MNPs concentrations (60 to 1000 µg/mL) at 24 h and 48 h. Data are mean ± S.D. expressed as % of control response. *Statistically different from control cell monolayers, using $p < 0.05$. Red dashed line threshold limited or cell viability (ISO 10993-5).

4. Conclusions

A simple co-precipitation method has been developed for the *in-situ* preparation of COS-coated magnetic Fe₃O₄ nanoparticles through a mixing of iron ions (Fe³⁺ and Fe²⁺) and COS aqueous solutions followed by precipitation with ammonia. The impact of the COS with different DP/DA (10/53, 24/24, 24/47 and 45/47) were evaluated on the synthesis and behaviors of coated NPs. The results showed that Fe₃O₄ nanoparticles were well encapsulated by all the used COS, without changing the crystalline structure. Thermogravimetric analysis permitted to estimate the organic content on the surface of Fe₃O₄ nanoparticles (11.25 % for Fe₃O₄:COS_{10/53}, 17.72 % for Fe₃O₄:COS_{24/24}, 15.14 % for Fe₃O₄:COS_{24/47} and 10.51 % for Fe₃O₄:COS_{45/47}). A convergent structural analysis revealed that the COS layer did not change significantly the particles size and all the synthesized NPs have diameters between 6 and 10 nm. The COS-coated nanoparticles showed a nearly spherical morphology with a narrower size distribution and a better dispersion than pure Fe₃O₄ MNPs. The presence of COS on the surface of Fe₃O₄ NPs contributed to structurally and magnetically stabilize these particles. VSM results indicated that the magnetic nanoparticles show a superparamagnetic-like behavior with negligible coercivity (H_c) and remanence (M_r). The COS-coated Fe₃O₄ MNPs showed an increase between 18 and 22% of saturation magnetization in comparison with the control sample (Fe₃O₄ NPs - 57.80 emu.g⁻¹). Several methods were used to determine the diameter of the particles and the results were in good agreement. A cytotoxicity study on canine fibroblasts showed that the cell viability of all magnetic nanoparticles depended on their concentration, and that the COS-

coated NPs permitted a better cell viability in comparison with pure Fe₃O₄ nanoparticles (an increase of 100% of the dose limit).

Although Fe₃O₄:COS nanoparticles presented interesting results, it is not straightforward to describe precisely the impact of COS structure on the NPs behaviors. We have shown that the nanoparticles coated by COS with DA ~ 50 % present a better cytocompatibility. It can be suggested that this fact is due to a different chain solubility and conformation at neutral pH. However, to better explain the intrinsic effect of the COS structure on the biological properties, the quantification of particle internalization is necessary. Summarizing, we were able to prepare functionalized ultra-small superparamagnetic-like nanoparticles exhibiting high saturation magnetization and an expressive cell viability enhancement. Additionally, free amino and hydroxyl groups on their surface allow designing a bio-functionalization of the nanoparticles to be used, for example, in magnetic-field assisted drug delivery, enzyme or cell immobilization and isolation, as well as a marker in cell tracking and other biomedical applications.

Acknowledgements

The Wide-angle X-ray detector (WOS) was funded by the French National Research Agency (ANR) under the "Investissement d'Avenir" program (Grant no. ANR-11-EQPX-0010). We thank ESRF and the CRG group for the opportunity to perform SAXS-WAXS measurements on beamline BM02. We also would like to thank the CTμ, *Plateforme de Microscopie Multidisciplinaire*, from Université Claude Bernard Lyon 1, for the support to realize the Transmission Electron Microscopy (TEM) analysis.

References

- [1] Gubin S, Koksharov Y, Khomutov G, Yurkov G 2005 Magnetic nanoparticles: Preparation methods, structure and properties *Uspekhi Khimii*, 74(6) 539-74.
- [2] Jun, Y-W, Huh Y-M, CHoi J-S, Lee J-H, Song H-T, KimKim, Yoon S, Kim K-S, Shin J-S, Suh J-S, Cheon J 2005 Nanoscale Size Effect of Magnetic Nanocrystals and Their Utilization for Cancer Diagnosis via Magnetic Resonance Imaging *J. Am. Chem. Soc.* 127(16) 5732-33.
- [3] Cardoso V F, Francesko A, Ribeiro C, Bañobre-López M, Martins P, Lanceros-Mendez S, 2017 Advances in Magnetic Nanoparticles for Biomedical Applications *Adv. Healthcare Mater.* 7(5) 1700845.
- [4] Lu A-H, Salabas E L, Shüth F, 2007 Magnetic Nanoparticles: Synthesis, Protection, Functionalization, and Application. *Angewandte Chemie International Edition*, 46(8) 1222-44.
- [5] Conte, M P, Sahoo J K, Abul-Haija Y M, Lau K H A, Ulijn R V, 2018 Biocatalytic Self-Assembly on Magnetic Nanoparticles *ACS Appl. Mater. Interfaces* 10(3) 3069-75.
- [6] Yallapu, M M, Othman S F, Curtis E T, Gupta B K, Jaggi M, Chauhan S C, 2011 Multi-functional magnetic nanoparticles for magnetic resonance imaging and cancer therapy *Biomaterials* 32(7) 1890-1905.
- [7] Wilhelm C, Gazeau F, 2008 Universal cell labelling with anionic magnetic nanoparticles. *Biomaterials* 29(22)3161-74.
- [8] Hao R, Xing R, Xu Z, Hou Y, Gao S, Sun S, 2010 Synthesis, Functionalization, and Biomedical Applications of Multifunctional Magnetic Nanoparticles *Adv. Mater.* 22(25) 2729-42.
- [9] Sun M, Liu Y, Shen Q-D, Jiang S, 2016 Dual-Color Fluorescence Imaging of Magnetic Nanoparticles in Live Cancer Cells Using Conjugated Polymer Probes *Sci. Rep.* 6 22368.
- [10] Mohammed L, Gomaa H G, Ragab D, Zhu J, 2017 Magnetic nanoparticles for environmental and biomedical applications: A review *Particuology* 30 1-14.
- [11] Ling D, Hyeon T, 2012 Chemical Design of Biocompatible Iron Oxide Nanoparticles for Medical Applications *Small* 9(9-10) 1450-66.
- [12] Boxall C, Kelsall G, Zhang Z, 1996 Photoelectrophoresis of colloidal iron oxides. Part 2.-Magnetite (Fe₃O₄) *J. Chem. Soc., Faraday Transactions* 92(5) 791-802.

- [13] Wu W, Wu Z, Yu T, Jiang C, Woo-Sik K, 2015 Recent progress on magnetic iron oxide nanoparticles: synthesis, surface functional strategies and biomedical applications *Sci. Technol. Adv. Mater.* 16(2) 023501.
- [14] Oldham J W, (R. T.) Shuey. 1975 Semiconducting ore minerals (Developments in Economic Geology, 4). Amsterdam and New York, Elsevier Sci. Publ. Co., 415.
- [15] Jun Y-W, Seo J-W, Cheon J, 2008 Nanoscaling Laws of Magnetic Nanoparticles and Their Applicabilities in Biomedical Sciences *Acc. Chem. Res.* 41(2) 179-89.
- [16] Sharifi S, Seyednejad H, Laurent S, Atyabi F, Saei A A, Mahmoudi M, 2015 Superparamagnetic iron oxide nanoparticles for in vivo molecular and cellular imaging. *Contrast Media Mol. Imaging* 10(5) 329-55.
- [17] Xu C, Sun S, 2013 New forms of superparamagnetic nanoparticles for biomedical applications *Adv. Drug Deliv. Rev.* 65(5) 732-43.
- [18] Ling D, Hyeon T, 2013 Chemical Design of Biocompatible Iron Oxide Nanoparticles for Medical Applications *Small* 9(9-10) 1450-66.
- [19] Chatterjee K, Sarkar S, Rao K J, Paria S, 2014 Core/shell nanoparticles in biomedical applications *Adv. Colloid Interface Sci.* 209 8-39.
- [20] Foglia S, Ledda M, Fioretti D, Iucci G, Papi M, Capellini G, Lolli M G, Grimaldi S, Rinaldi M, Lisi A, 2017 In vitro biocompatibility study of sub-5 nm silica-coated magnetic iron oxide fluorescent nanoparticles for potential biomedical application *Sci. Rep.* 7 46513.
- [21] Bourrinet P, Bengel H H, Bonnemain B, Dencausse A, Idee J-M, Jacobs P M, Lewis J M, 2006 Preclinical Safety and Pharmacokinetic Profile of Ferumoxtran-10, an Ultrasmall Superparamagnetic Iron Oxide Magnetic Resonance Contrast Agent *Investig. Radiol.* 41(3).
- [22] Abakumov M A, Semkina A S, Skorikov A S, Vishnevskiy D A, Ivanova A V, Mironova E, Davydova G A, Majouga A G, Chekhonin V P, 2018 Toxicity of iron oxide nanoparticles: Size and coating effects *J. Biochem. Mol. Toxicol.* 32(12) e22225.
- [23] Kania G, Sternak M, Jaształ A, Chlopicki S, Błażejczyk A, Nasulewicz-Goldeman A, Wietrzyk J, Jasiński K, Skórka T, Zapotoczny S, Nowakowska M, 2017 Uptake and bioreactivity of charged chitosan-coated superparamagnetic nanoparticles as promising contrast agents for magnetic resonance imaging *Nanomedicine: NBM* 14(1) 131-40.
- [24] Stepanov A, Fedorenko S, Amirov R, Nizameev I, Kholin K, Voloshina A, Sapunova A, Mendes R, Rummeli M, Gemming T, Mustafina A, Odintsov B, 2018 Silica-coated iron-oxide nanoparticles doped with Gd(III) complexes as potential double contrast agents for magnetic resonance imaging at different field strengths *J. Chem. Sci.* 130(9) 125.
- [25] Peter M G, 1995 Applications and Environmental Aspects of Chitin and Chitosan *J. Macromol. Sci A* 32(4) 629-40.
- [26] Rinaudo M, 2006 Chitin and chitosan: Properties and applications *Prog. Polym. Sci.* 31(7) 603-32.
- [27] Younes I, Rinaudo M, 2015 Chitin and Chitosan Preparation from Marine Sources. Structure, Properties and Applications *Mar. Drugs* 13(3) 1133.
- [28] Liaqat F, Eltem R, 2018 Chitoooligosaccharides and their biological activities: A comprehensive review *Carbohydr. Polym.* 184 243-59.
- [29] Tsai G-J, Zhang S-L, Shieh P-L, 2004 Antimicrobial Activity of a Low-Molecular-Weight Chitosan Obtained from Cellulase Digestion of Chitosan *J. Food Protec.* 67(2) 396-98.
- [30] Guo Z, Xing R, Liu S, Zhong Z, Ji X, Wang L, Li P, 2008 The influence of molecular weight of quaternized chitosan on antifungal activity *Carbohydr. Polym.* 71(4) 694-97.
- [31] Xia W, Liu P, Zhang J, hen J, 2011 Oligosaccharides. *Food Hydrocoll.* 25(2) 170-79.
- [32] Huang J, Wang L, Zhong X, Li Y, Yang L, Mao H, 2014 Facile non-hydrothermal synthesis of oligosaccharide coated sub-5 nm magnetic iron oxide nanoparticles with dual MRI contrast enhancement effects. *J. Mater. Chem. B* 2(33)5344-51.
- [33] Shukla S, Jadaun A, Arora V, Sinha R K, Biyani N, Jain V K, 2015 In vitro toxicity assessment of chitosan oligosaccharide coated iron oxide nanoparticles *Toxicol. Rep.* 2 27-39.

- [34] Le Thi T N, Nguyen T H, Hoang D Q, Tran T V, Nguyen N T, Nguyen D H, 2017 Development of new magnetic nanoparticles: Oligochitosan obtained by γ -rays and γ -coated Fe₃O₄ nanoparticles *Appl. Surf. Sci.* 422(Supplement C) 863-68.
- [35] Huang Y, Gong J, Zhang Q, Hua M, Wu J, 2016 Synthesis and characterization of low molecular weight chitosan decorated Fe₃O₄ nanoparticles as T2 contrast agent *Mater. Chem. Phys.* 180 122-27.
- [36] Bae K H, Park M, Do M J, Lee N, Ryu J H, Kim G W, Kim C, Park T G, Hyeon T, 2012 Chitosan Oligosaccharide-Stabilized Ferrimagnetic Iron Oxide Nanocubes for Magnetically Modulated Cancer Hyperthermia *ACS Nano* 6(6) 5266-73.
- [37] Hirai A, Odani H, Nakajima A, 1991 Determination of degree of deacetylation of chitosan by ¹H NMR spectroscopy. *Polym. Bull.* 26(1) 87-94.
- [38] Salim E, Ailincal D, Trombotto S, 2014 Chitooligosaccharide-2,5-anhydro-D-mannonic Acid *Molbank* Vol. 2014.
- [39] Vårum K M, Antohonsen M W, Grasdalen H, Smidsrød O, 1991 Determination of the degree of N-acetylation and the distribution of N-acetyl groups in partially N-deacetylated chitins (chitosans) by high-field n.m.r. spectroscopy *Carbohydr. Res.* 211(1) 17-23.
- [40] Chahine A G, Blanc N, Arnaud S, De Geuser F, Guinebretière R, Boudet N, 2019 Advanced Non-Destructive in Situ Characterization of Metals with the French Collaborating Research Group D2AM/BM02 Beamline at the European Synchrotron Radiation Facility *Metals* 9(3).
- [41] Cótica LF, Estrada F R, Freitas V F, Dias G S, Santos I A, Eiras J A, Garcia D, 2012 Ferroc states in La doped BiFeO₃-PbTiO₃ multiferroic compounds *J. Appl. Phys.* 111(11) 114105.
- [42] de Britto D, Campana-Filho S P, 2004 A kinetic study on the thermal degradation of N,N,N-trimethylchitosan *Polym. Degrad. Stabil.* 84(2) 353-61.
- [43] Focher B, Beltrame P L, Naggi A, Torri G, 1990 Alkaline N-deacetylation of chitin enhanced by flash treatments. Reaction kinetics and structure modifications *Carbohydr. Polym.* 12(4) 405-18.
- [44] Focher B, Naggi A, Torri G, Cosani A, Terbojevich M, 1992 Chitosans from *Euphausia superba*. 2: Characterization of solid state structure *Carbohydr. Polym.* 18(1) 43-9.
- [45] Zajac A, Hanuza J, Wandas M, Dymińska L, 2015 Determination of N-acetylation degree in chitosan using Raman spectroscopy. *Spectrosc. Acta A* 134 114-20.
- [46] Duarte M L, Ferreira M C, Marvão M R, Rocha J, 2002 An optimised method to determine the degree of acetylation of chitin and chitosan by FTIR spectroscopy *Int. J. Biol. Macromol.* 31(1) 1-8.
- [47] Waldron R D, 1955 Infrared Spectra of Ferrites *Phys. Rev.* 99(6) 1727-35.
- [48] Ma M, Zhang Y, Yu W, Shen H, Zhang H, Gu N, 2003 Preparation and characterization of magnetite nanoparticles coated by amino silane *Colloid. Surf. A-Physicochem. Eng. Asp.* 212(2-3) 219-226.
- [49] Monazam E R, Breault R W, Siriwardane R, 2014 Kinetics of Magnetite (Fe₃O₄) Oxidation to Hematite (Fe₂O₃) in Air for Chemical Looping Combustion *Ind. Eng. Chem. Res.* 53(34) 13320-28.
- [50] Grimm S, Schultz M, Barth S, Muller R, 1997 Flame pyrolysis – a preparation route for ultrafine pure γ -Fe₂O₃ powders and the control of their particle size and properties *J. Mater. Sci.* 32(4) 1083-92.
- [51] Cornell R M, Schwertmann U, 2003 *The Iron Oxides: Structure, Properties, Reactions, Occurrences and Uses*. Second ed., Weinheim: Wiley-VCH.
- [52] Kodama R, 1999 Magnetic nanoparticles *J. Magn. Magn. Mater.* 200(1-3) 359-72.
- [53] Coey J M D, 1971 Noncollinear Spin Arrangement in Ultrafine Ferrimagnetic Crystallites *Phys. Rev. Lett.* 27(17) 1140-42.
- [54] Mazo-Zuluaga J, Restrepo J, Mejía-López J, 2008 Effect of surface anisotropy on the magnetic properties of magnetite nanoparticles: A Heisenberg–Monte Carlo study *J. Appl. Phys.* 103(11) 113906.
- [55] Oliveira P N, Bini R D, Dias G S, Alcouffe P, Santos I A, David L, Cótica L F, 2018 Magnetite nanoparticles with controlled sizes via thermal degradation of optimized PVA/Fe(III) complexes. *J. Magn. Magn. Mater.* 460 381-90.

- [56] Unsoy G, Yalcin S, Khodadust R, Gunduz G, Gunduz U, 2012 Synthesis optimization and characterization of chitosan-coated iron oxide nanoparticles produced for biomedical applications *J. Nanopart. Res.* 14(11) 964.
- [57] Bodker F, Morup S, 2000 Size dependence of the properties of hematite nanoparticles *Europhys. Lett.* 52(2) 217-23.
- [58] Jamet M, Dupuis V, Mélinon P, Guiraud G, Pérez A, Wernsdorfer W, Traverse A, Baguenard B, 2000 Structure and magnetism of well defined cobalt nanoparticles embedded in a niobium matrix *Phys. Rev. B* 62(1) 493-99.
- [59] Ferrari E F, da Silva F C S, Knobel M, 1997 Influence of the distribution of magnetic moments on the magnetization and magnetoresistance in granular alloys *Phys. Rev. B* 56(10) 6086-93.
- [60] Cotica L F, Santos I A, Giroto E M, Ferri E V, Coelho A A, 2010 Surface spin disorder effects in magnetite and poly(thiophene)-coated magnetite nanoparticles *J. Appl. Phys.* 108(6).
- [61] Hussain R F, Nouri A M E, Oliver R T D, 1993 A new approach for measurement of cytotoxicity using colorimetric assay. *J. Immunol. Methods* 160(1) 89-96.
- [62] Van Ta Q, Kim M-M, Kim S-K, 2006 Inhibitory Effect of Chitooligosaccharides on Matrix Metalloproteinase-9 in Human Fibrosarcoma Cells (HT1080) *Mar. Biotechnol.* 8(6) 593-99.
- [63] Mao S, Shuai X, Unger F, Simon M, Bi D, Kissel T, 2004 The depolymerization of chitosan: effects on physicochemical and biological properties *Int. J. Pharm.* 281(1) 45-54.
- [64] Lv X, Liu Y, Song S, Tong C, Shi X, Zhao Y, Zhang J, Hou M, 2019 Influence of chitosan oligosaccharide on the gelling and wound healing properties of injectable hydrogels based on carboxymethyl chitosan/alginate polyelectrolyte complexes *Carbohydr. Polym.* 205 312-21.
- [65] Jadhav S V, Kim N B M, Lee H Y, Im I C, 2018 Induction heating and in vitro cytotoxicity studies of MnZnFe₂O₄ nanoparticles for self-controlled magnetic particle hyperthermia *J. Alloys Compd.* 745 282-91.
- [66] Shahabadi N, Akbari A, Karampour F, Falsafi M, 2019 Cytotoxicity and antibacterial activities of new chemically synthesized magnetic nanoparticles containing eugenol *J. Drug Deliv. Sci. Tec.* 49 113-22.
- [67] Yang N, Li W-H, 2015 Preparation of gold nanoparticles using chitosan oligosaccharide as a reducing and capping reagent and their in vitro cytotoxic effect on Human fibroblasts cells *Mater. Lett.* 138 154-57.
- [68] Jenkins G J S, Asadi R, Doak S H, 2010 Potential toxicity of superparamagnetic iron oxide nanoparticles (SPION) AU - Singh, Neenu *Nano Rev.* 1(1) 5358.
- [69] Kumar V, Sharma N, Maitra S S, 2017 In vitro and in vivo toxicity assessment of nanoparticles *Int. Nano Lett.* 7(4) 243-56.
- [70] Mahmoudi M, Simchi A, Shokrgozar M A, Milani A S, Häfeli U O, Stroeve P, 2010 A new approach for the in vitro identification of the cytotoxicity of superparamagnetic iron oxide nanoparticles *Colloids Surf B: B* 75(1) 300-9.

Supporting Material

***In situ* synthesis of Fe₃O₄ nanoparticles coated by chito-oligosaccharides: physico-chemical characterizations and cytotoxicity evaluation for biomedical applications**

Paula Nunes de Oliveira^{*1}, Amani Moussa¹, Nadège Milhau², Raquel Dosciatti Bini³, Caroline Prouillac², Breno Ferraz de Oliveira³, Gustavo Sanguino Dias³, Ivair Aparecido Santos³, Isabelle Morfin⁴, Guillaume Sudre¹, Pierre Alcouffe¹, Thierry Delair¹, Luiz Fernando Cótica³, Stéphane Trombotto¹, Didier Pin², Laurent David¹.

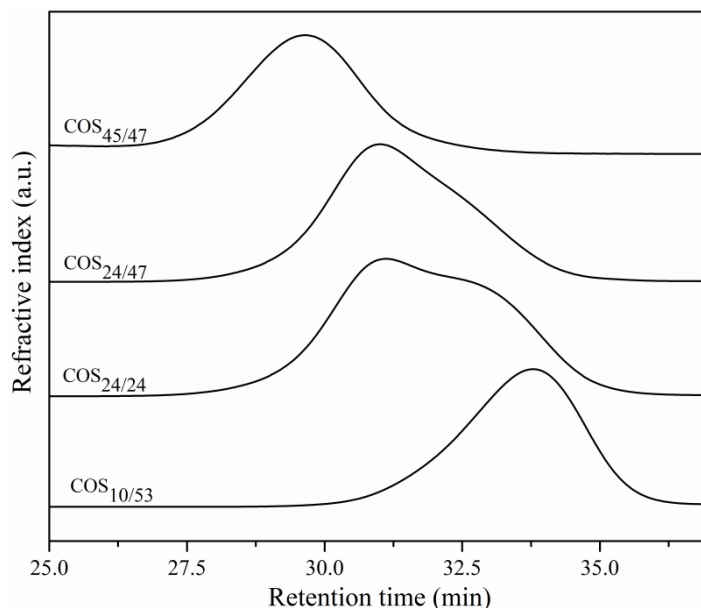
¹IMP, CNRS UMR 5223, Univ Claude Bernard Lyon 1, Univ Lyon, 15 bd Latarjet, 69622 Villeurbanne, FR

²Université de Lyon, VetAgro Sup, Unité ICE, 1 av. Bourgelat, 69280 Marcy L'Etoile, FR

³Department of Physics, State University of Maringá, Av. Colombo, 5790, Maringá, Paraná, BR, 87020-900

⁴Université Grenoble Alpes, LiPhy, 38000 Grenoble FR

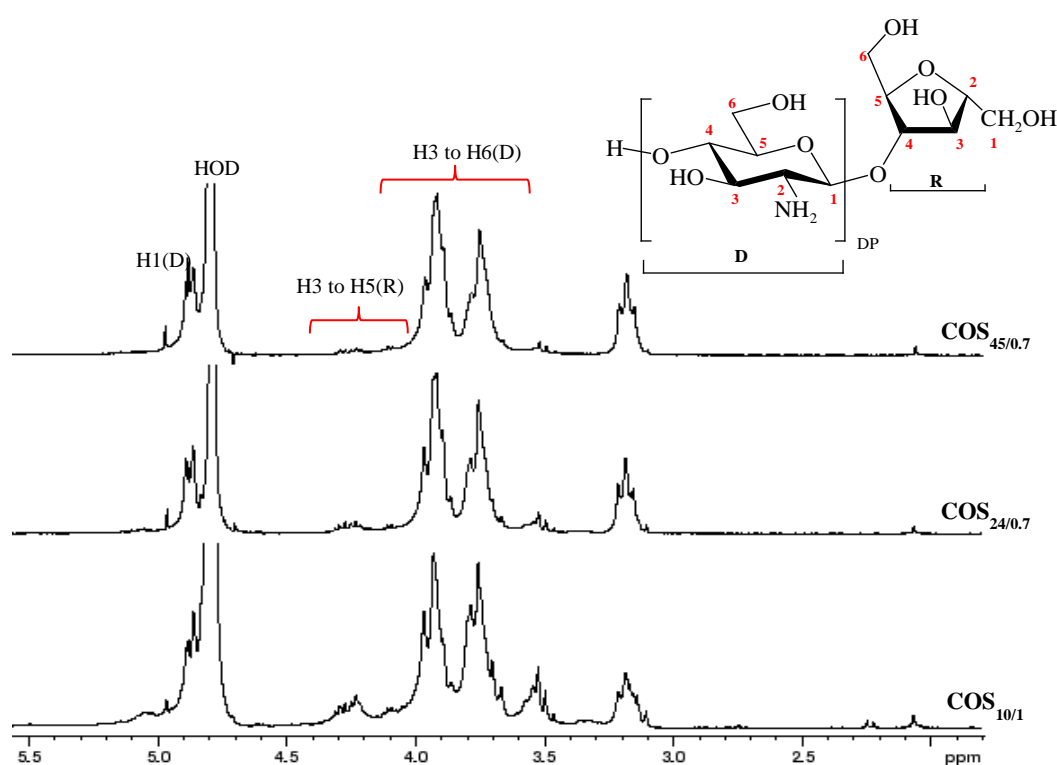
*paulaoliveiraqmc@gmail.com



SM-Figure 1 - Size exclusion chromatograms (AcOH (0.2 M)/AcONH₄ (0.15 M) buffer, pH 4.5) for COS_{10/53}, COS_{24/24}, COS_{24/47} and COS_{45/47} samples.

For COS_{10/1}, COS_{24/0.69} and COS_{45/0.71} samples, the average GlcN repeating unit number \overline{DP} , given in Table 1, was determined by ¹H-NMR spectroscopy (see SM-Figure 2) from the relative peak intensities of H-4 (anhydro manofuranose-amf) and H-2 (GlcN) signals at 4.23 and 3.15 ppm, respectively, according to the Equation (1):

$$\overline{DP} = \frac{I_{H-2} \text{ (GlcN)}}{I_{H-4} \text{ (reduced amf)}} \quad \text{Eq.(1)}$$



SM-Figure 2 - ^1H NMR spectra (500 MHz, 298 K) of $\text{COS}_{10/1}$, $\text{COS}_{24/0.7}$ and $\text{COS}_{45/0.7}$ samples in D_2O and $5\mu\text{l}$ of HCl .

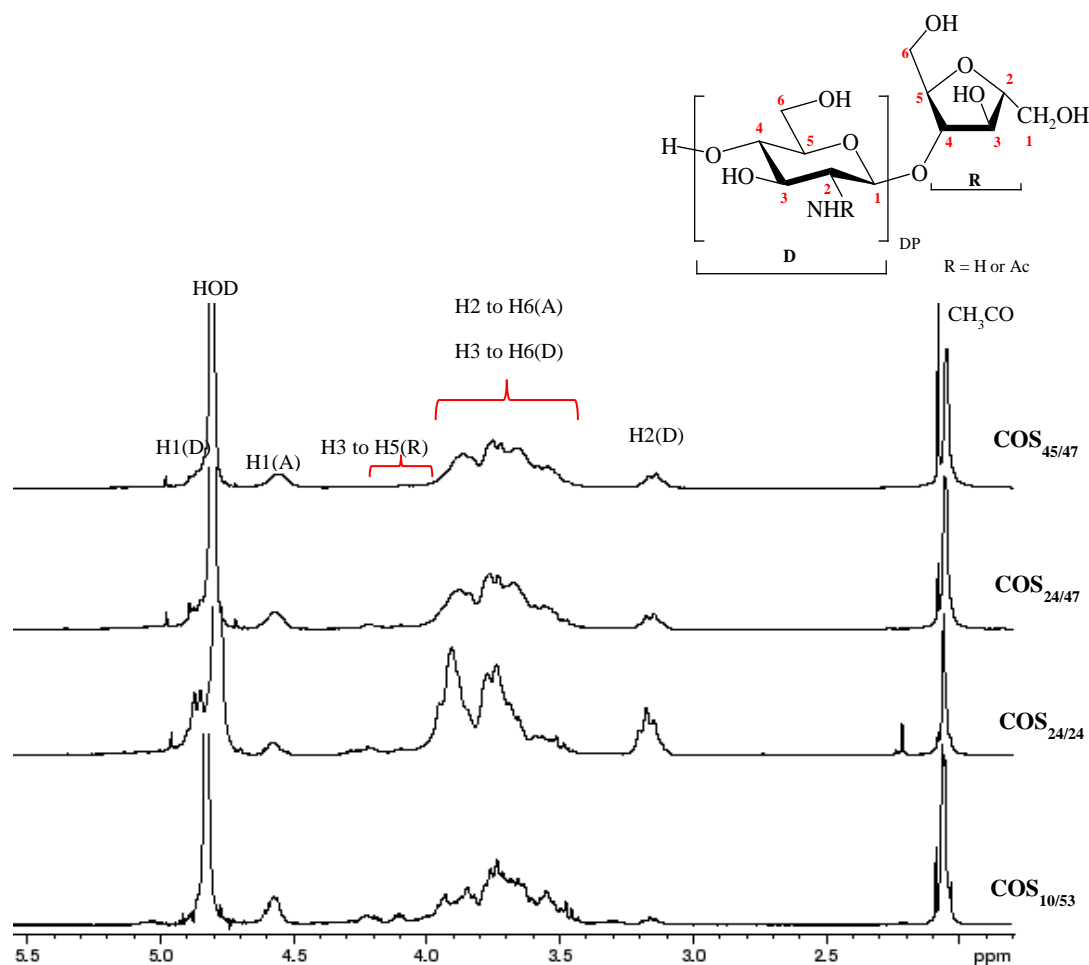
For SEC-MALLS chromatography the average DP was calculated according to the number-average molar mass (\overline{Mn}) of reduced chitooligosaccharides, the molar mass of the GlcN repeating unit ($M_0 = 161\text{g/mol}$) and molar mass of the reduced anhydro manofuranose (amf) unit ($M_{(\text{reduced amf})} = 164\text{g/mol}$) according to Equation 2 (see results in Table 1).

$$\overline{DP} = \frac{\overline{Mn} - M(\text{reduced amf})}{M_0} \quad \text{Eq. (2)}$$

The average DA of the different acetylated samples was determined by considering both signal areas of H2 protons of GlcN units ($I_{\text{GlcN-H}_2}$) and acetyl protons of GlcNAc units (I_{CH_3}) according to Equation 3 [1]. It was remarkable that the presence of acetic acid peaks was close to the signal of the acetyl groups (see SM-Figure 3). Of course, this was taken into consideration when calculating the DA and this area was not considered.

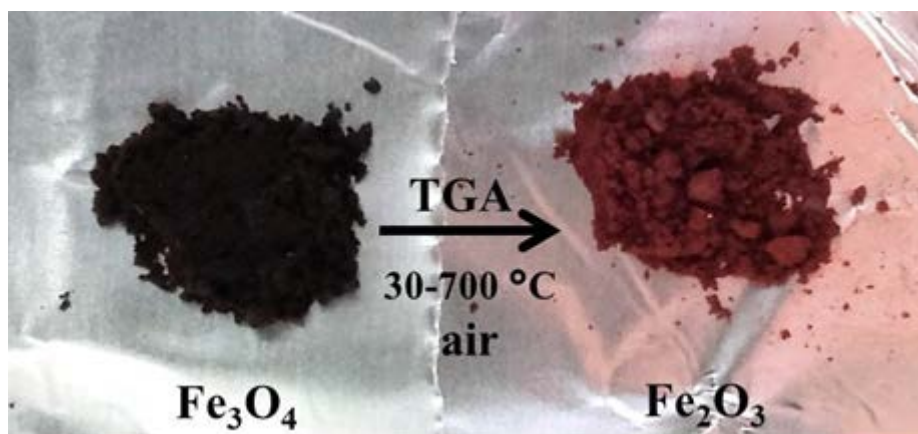
$$\text{DA (\%)} = \frac{\left(\frac{1}{3}\right) \times I_{\text{CH}_3}}{\left(\frac{1}{3}\right) I_{\text{CH}_3} + I_{\text{GlcN-H}_2}} \times 100 \quad \text{Eq. (3)}$$

Additionally, samples were also characterized by SEC-MALLS according to their mass- and number-average molar mass and dispersity, \overline{M}_w , \overline{M}_n and \overline{D} , respectively (Table 1).

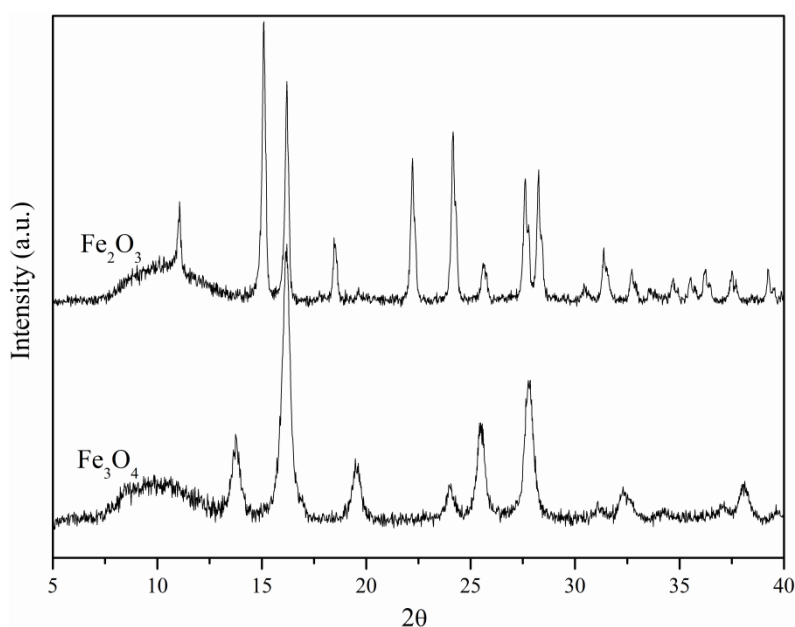


SM-Figure 3 - ^1H NMR spectra (500 MHz, 298 K) for $\text{COS}_{10/53}$, $\text{COS}_{24/24}$, $\text{COS}_{24/47}$ and $\text{COS}_{45/47}$ samples in D_2O and 5 μl of HCl.

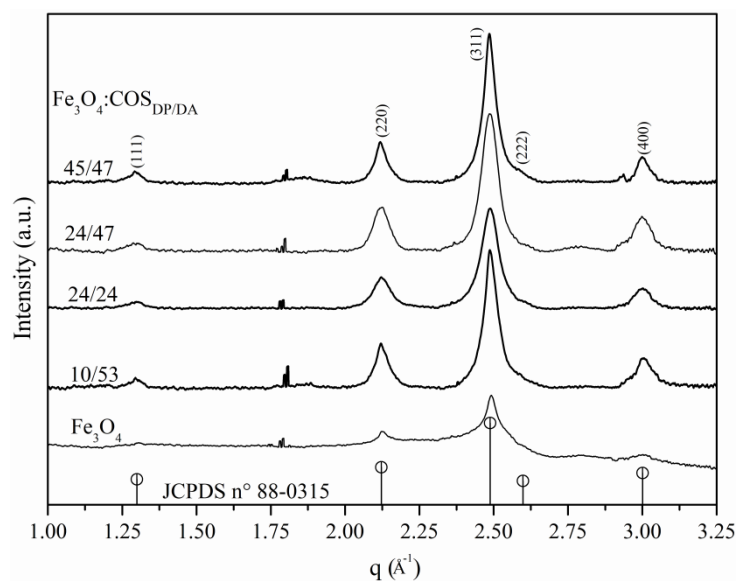
The average DP for the acetylated oligomers, was calculated according to the number-average molar mass (\overline{M}_n) of the partially *N*-acetylated reduced chito-oligosaccharides, the molar mass of the reduced amf unit ($M_{(\text{reduced amf})} = 164 \text{ g/mol}$) and the molar mass of the GlcN repeating unit (M_0). However in this case M_0 depends on the DA, hence in Equation 3, M_0 includes the molar mass of the GlcN/GlcNAc unit ($M_{(\text{GlcN})} = 161$ and $M_{(\text{GlcNAc})} = 203 \text{ g/mol}$). The results are demonstrated in Table 1. Their characterization shows that their molar mass distribution \overline{D} is rather narrow. The details for the calculations of \overline{DP} and \overline{DA} are given in Table 1.



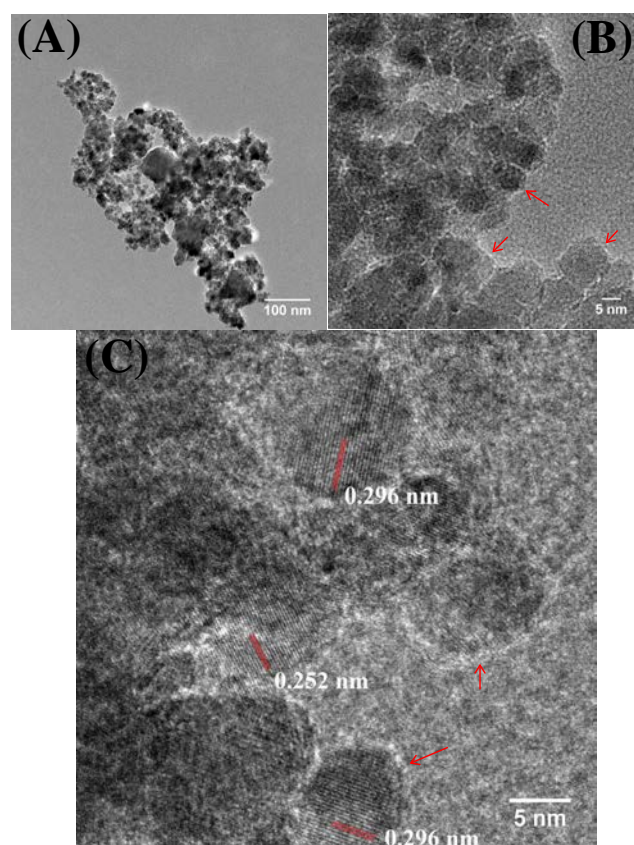
SM- Figure 4 – Initial Fe_3O_4 nanoparticles (black) before the TGA experiment, (*i.e.* heating at $10\text{ }^\circ\text{C min}^{-1}$, under air from 30 to $700\text{ }^\circ\text{C}$) and Fe_2O_3 particles (final product - red).



SM-Figure 5 – The structure of the magnetite nanoparticles (Fe_3O_4) and hematite (Fe_2O_3) particles were examined by X-ray diffraction (XRD). The Fe_2O_3 is the product formed after the submission of Fe_3O_4 samples pass for the TGA analysis (under air atmosphere). The XRD patterns were recorded in a Shimadzu XRD 7000 equipped with Mo-K_α radiation ($\lambda = 0.7107\text{ \AA}$), in the scattering angle 2θ from 5° to 40° .



SM-Figure 6 – WAXS curves for Fe₃O₄ and Fe₃O₄:COs_{DP/DA} nanoparticles and comparison with JCPDS n° 88-0315 card.



SM-Figure 7 – HR-TEM images of the Fe₃O₄:COs_{45/47} nanoparticles at different magnification (A and B) and (C) shows the diffraction plans at 0.296 nm and 0.252 nm and they are in good agreement with the planes (220) and (311) of the cubic magnetite, respectively. Red arrows indicate whiter

zones indicating the possible presence of COS on the surface of nanoparticles. The experiment was performed using a High-Resolution Transmission Electron Microscopes JEOL 2100F. The nanoparticle suspension was prepared in deionized water and submitted to ultrasonic bath for 10 min, then dropped on the grid and the solvent dried at room temperature.

References

1. Trombotto S, Ladaviere C, Delolme F, Domard A. Chemical Preparation and Structural Characterization of a Homogeneous Series of Chitin/Chitosan Oligomers 2008, *Biomacromolecules*. 2008, 9, 1731-8.